J. Membrane Biol. 176, 77–100 (2000)
DOI: 10.1007/s00232001077

The Journal of
Membrane
Biology

HCO_3^- Transport in a Mathematical Model of the Pancreatic Ductal Epithelium

Y. Sohma[1], M.A. Gray[2], Y. Imai[1], B.E. Argent[2]
[1]Department of Physiology, Osaka Medical College, Takatsuki, Osaka 569-8686, Japan
[2]Department of Physiological Sciences, University Medical School, Framlington Place, Newcastle upon Tyne NE2 4HH, UK

Received: 15 November 1999/Revised: 29 March 2000

Abstract. We have used computer modeling to investigate how pancreatic duct cells can secrete a fluid containing near isotonic (~140 mM) $NaHCO_3$. Experimental data suggest that $NaHCO_3$ secretion occurs in three steps: (i) accumulation of HCO_3^- across the basolateral membrane of the duct cell by $Na(HCO_3)_n$ cotransporters, Na^+/H^+ exchangers and proton pumps; (ii) secretion of HCO_3^- across the luminal membrane on Cl^-/HCO_3^- antiporters operating in parallel with Cl^- channels; and (iii) diffusion of Na^+ through the paracellular pathway. Programming the currently available experimental data into our computer model shows that this mechanism for HCO_3^- secretion is deficient in one important respect. While it can produce a relatively large volume of a HCO_3^--rich fluid, it can only raise the luminal HCO_3^- concentration up to about 70 mM. To achieve secretion of 140 mM $NaHCO_3$ by the model it is necessary to: (i) reduce the conductive Cl^- permeability and increase the conductive HCO_3^- permeability of the luminal membrane of the duct cell, and (ii) reduce the activity of the luminal Cl^-/HCO_3^- antiporters. Under these conditions most of the HCO_3^- is secreted via a conductive pathway. Based on our data, we propose that HCO_3^- secretion occurs mainly by the antiporter in duct segments near the acini (luminal HCO_3^- concentration up to ~70 mM), but mainly via channels further down the ductal tree (raising luminal HCO_3^- to ~140 mM).

Key words: Pancreatic duct cells — Mathematical model — HCO_3^- secretion — Cl^- secretion — Cystic fibrosis transmembrane conductance regulator

Introduction

The ductal epithelial cells of the pancreas form a network of branching tubules whose function is to convey digestive enzymes secreted by the acinar cells into the intestine [for reviews *see* 4, 5]. The ducts also secrete an alkaline fluid, rich in $NaHCO_3$, which washes the digestive enzymes down the ductal tree and also partially neutralizes acid chyme entering the duodenum from the stomach. The maximum concentration of HCO_3^- found in pancreatic juice depends on the species, and varies between about 70 mM in the rat and 145 mM in guinea pig, cat, dog and human [4, 5 for reviews].

As a result of electrophysiological and spectrofluorometric studies performed largely on small interlobular and intralobular ducts isolated from the rat pancreas, an HCO_3^- secretory model has been proposed (*see* Fig. 1) [4, 5 for reviews]. The model is largely based on the localization of transport elements in the duct cell, and the way in which they respond when HCO_3^- secretion is stimulated. In brief, the initial step in HCO_3^- secretion is accumulation of the anion across the basolateral membrane of the duct cell. This is achieved by backward transport of protons (Na^+/H^+ exchanger and proton pump) and forward transport of HCO_3^- ions (Na^+-HCO_3^- cotransporter). Once accumulated inside the duct cell, the HCO_3^- ion is then secreted across the luminal membrane on a Cl^-/HCO_3^- exchanger. The rate at which the exchangers cycle is thought to be controlled by the opening of Cl^- channels on the luminal plasma membrane. To date, cyclic AMP-activated, CFTR Cl^- channels and Ca^{2+}-activated Cl^- channels have been identified on the luminal membrane of the duct cell. These ion channels are key regulatory points in the HCO_3^- secretory mechanism and can be viewed as having two roles: (i) to provide luminal chloride for operation of the anion exchanger, and (ii) to dissipate the intracellular Cl^- that accumulates as the exchangers cycle. Since the CFTR channels have a low permeability to HCO_3^- relative to Cl^- (about 1:5), it was originally thought that little HCO_3^- could be secreted directly via the conductance pathway.

One problem with the scheme described above is that with near isotonic $NaHCO_3$ in the duct lumen (as

Correspondence to: Y. Sohma

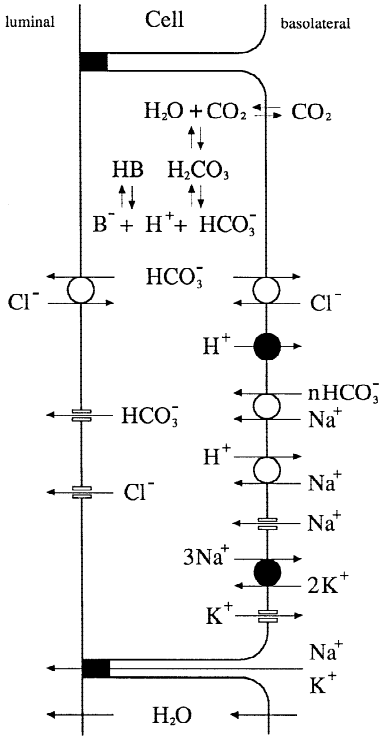

Fig. 1. Schematic representation of the ion transport systems in our mathematical model of an intact pancreatic duct. For illustrative purposes, the Cl^- and HCO_3^- conductances on the apical membrane are represented as separate pathways.

occurs in most species except the rat), the concentration of Cl^- in the luminal fluid will be very low (~10 mM). This means that given reasonable values for intracellular $[HCO_3^-]$, the intracellular Cl^- concentration would have to be very low indeed (<1 mM) to drive HCO_3^- secretion on a luminal Cl^-/HCO_3^- exchanger. Thus while the model described above and shown in Fig. 1 might describe how the rat pancreas works (maximum juice $[HCO_3^-]$ about 70 mM), at first sight it cannot explain how near isotonic HCO_3^- is secreted by species such as the guinea pig, cat, dog and man. Some workers have suggested that there are differences in the HCO_3^- secretory mechanism between low (rat) and high $[HCO_3^-]$ (guinea pig) secretors [23, 24]. However, in our view the evidence for such differences is not strong. Indeed, far from identifying differences between rat and guinea-pig duct cells, recent publications have emphasized the similarities in terms of the key transport elements that are involved in HCO_3^- secretion. Both species have basolateral Na^+-HCO_3^- cotransporters [rat: 46; guinea pig: 23, 9], Na^+/H^+ exchangers [rat: 46, 28, 41; guinea pig: 23, 9] and H^+ pump [rat: 46; guinea pig: 9], together with Cl^-/HCO_3^- antiporters [rat: 46, 29; guinea pig: 24] and Cl^- channels [rat: 11, 15; guinea pig: 31] in their luminal membrane. Moreover, it is possible that the low $[HCO_3^-]$ in rat pancreatic juice reflects a high rate of secondary anion exchange (luminal HCO_3^- for blood Cl^-) in the ductal system of this species, rather than a low $[HCO_3^-]$ in the primary fluid secreted by the duct cells. We believe the challenge now is to understand how the pancreatic ductal system can secrete an isotonic HCO_3^- solution within the framework of the basic scheme shown in Fig. 1.

Our approach to this problem has been to develop a computer model of the duct cell, the first version of which was published in 1996 [36]. The utility of this approach is that the mathematical model can be used in a predictive way, allowing hypothesis to be set up which can be tested experimentally. Our model provides information about secretory rate and the HCO_3^- concentration in the secreted fluid, as well as transient and steady-state data on intracellular pH and $[Cl^-]$, membrane and transepithelial potentials, and the voltage divider ratio. Because the first version of the model [36] was based on early data obtained from rat ducts, it did not consider diffusive HCO_3^- permeability on the luminal membrane and included only Na^+/H^+ exchangers for the basolateral acid-base transporters. Therefore, we have developed a new program that includes all the transport elements shown in Fig. 1.

In this paper we have investigated how the transport parameters must be altered to allow the new model cell to secrete isotonic $NaHCO_3$. Based on our results we have developed a new hypothesis regarding the secretion of a HCO_3^--rich pancreatic juice which we believe resolves most of the controversial issues surrounding the current secretory mechanism. Some of our data have been presented in preliminary form [37].

Materials and Methods

Symbols

Subscripts

k: Compartment. *l*: luminal, *c*: intracellular, *bl*: basolateral.
m: Membrane (pathway). *l*: luminal, *bl*: basolateral, *j*: junctional.
i: Solute. *X*: total of solutes impermeable to membrane.

Compartment Variables

$c_i^{(k)}$, $[i]_{(k)}$: Concentration of solute *i* in a compartment (*k*).
$\pi_{(k)}$: Osmotic pressure in a compartment (*k*).
$Osm_{(k)}$: Osmolarity in a compartment (*k*).
$p_{(k)}$: Static pressure in a compartment (*k*).
$Vol_{(k)}$: Volume per 1 cm^2 epithelium of a compartment (*k*).
$E_{(k)}$: Electrical potential of a compartment (*k*).

Compartment Parameters

$C_{p(k)}$: Compliance of a compartment (*k*).
$C_{e(k)}$: Electrical capacitance of a compartment (*k*).

Membrane Parameters

$A_{(m)}$: Area of a membrane (m) per 1 cm^2 epithelium, cm^2.
$Lp_{(m)}$: Water permeability of a membrane (m) per 1 cm^2 membrane.
$\omega_{i(m)}$: Permeability coefficient of solute i per 1 cm^2 membrane (m).
$G_{Na/H}$: Permeability coefficient for Na^+/H^+ antiporter.
$G_{Cl/HCO3(m)}$: Permeability coefficient for Cl^-/HCO_3^- antiporter on membrane (m).
K_i: Dissociation constant for binding of solute i to its site on the antiporter.
$G_{Na\text{-}HCO3}$: Permeability coefficient for Na^+-HCO_3^- cotransporter.
K_{ci}: Dissociation constant for binding of solute i to its site on the cotransporter.
$R_{l/k}$: Velocity constant ratio of cross-membrane steps in kinetics of Na^+-HCO_3^- cotransporter.
n_{co}: coupling ratio of HCO_3^- ion to a Na^+ ion in the Na^+-HCO_3^- cotransporter.
zL: Effective charge of the unloaded carrier.
$G_{NaKpump}$: Permeability coefficient for Na^+/K^+ pump.
$E_{NaKprev}$: Apparent reversal potential of Na^+/K^+ pump current over the physiological range.
K_{NaKpi}: Dissociation constant for binding of solute i to its site on the Na^+/K^+ pump.
G_{Hpump}: Permeability coefficient for H^+ pump.
$K_{Hp(k)}$: Dissociation constant for binding of H^+ to its site at facing to the compartment (k) on the H^+ pump.
$R_{lf/k}$ and $R_{lb/k}$: Velocity constant ratio of forward and backward reaction of the 'ATP' step to the 'non-ATP' step respectively, in the kinetics of H^+ pump.
n_{Hp}: number of H^+ carried by a single turnover in the H^+ pump.

Buffering Parameters

K_{CO2}: Dissociation constant of HCO_3^-/CO_2 buffering system.
K_{HB}: Dissociation constant of intrinsic buffering system.

Fluxes and Flows

$J_{v(m)}$: Water flux through a membrane (m).
$J_{i(m)}$: Total flux of solute i through a membrane (m).
$J_{e(m)}$: Total flux of positive charge through a membrane (m).
$J_{di(m)}$: Flux of solute i through diffusion pathway in a membrane (m).
$J_{Na/H}$: Turnover rate of the Na^+/H^+ antiporter.
$J_{Cl/HCO3(m)}$: Turnover rate of the Cl^-/HCO_3^- antiporter on membrane (m).
$J_{Na\text{-}HCO3}$: Turnover rate of the Na^+-HCO_3^- cotransporter.
$J_{NaKpump}$: Turnover rate of the Na^+/K^+ pump.
J_{Hpump}: Turnover rate of the H^+ pump.
$Flw_{v(k)}$: Net water influx into a compartment (k).
$Flw_{i(k)}$: Net influx of solute i into a compartment (k).
$Flw_{e(k)}$: Net influx of positive charge into a compartment (k).

Fluid Secretion

J_{vfld}: Rate of the fluid secretion from model epithelium.
$[HCO_3^-]_{fld}$: Effective HCO_3^- concentration of the secreted fluid.

Constants

dt: Integration intervals.
z_i: Valence of solute i.
R: Molar gas constant.
T: Absolute temperature.
F: Faraday's constant.
Δ: Difference.

The Model

Our new mathematical model of the pancreatic duct cell comprised the transport elements shown in Fig. 1. We unified the intact duct and single-cell versions of our previous model [36], into a three-compartment model simulating an epithelial cell *in situ* within an intact duct (Fig. 1). The model was based on experimental data obtained from microelectrode and fluorescent dye studies on microperfused ducts [28, 29, 30, 46], and fluorescent dye and patch-clamp studies performed on nonperfused ducts and on single duct cells [11, 12, 13, 15, 23, 24, 41, 43].

Variables

The model variables included $[Na^+]$, $[K^+]$, $[Cl^-]$, $[HCO_3^-]$ and pH in luminal, cellular and basolateral compartments, membrane potential, and cell volume. The cell volume (Vol_{cell}) and luminal, basolateral and transepithelial potential differences (PD_l, PD_{bl} and PD_{te}) are defined as we have previously described [36].

Model Equations

The mathematical model simulates membrane transport and cellular buffering systems in the duct cell. The membrane transport system in the mathematical model (Fig. 1) includes the following parameters: cell membrane water permeability, luminal Cl^- and HCO_3^- conductances and Cl^-/HCO_3^- antiporter, basolateral K^+ and Na^+ conductances, Na^+/H^+ antiporter, Na^+-HCO_3^- cotransporter, H^+-pump and Na^+/K^+-pump and paracellular nonselective cation conductance. The intracellular buffering system contains intracellular HCO_3^-/CO_2 buffering and intrinsic non-CO_2 buffering systems. It was assumed that all the parameters in the transport and buffering equations remained constant during simulations.

(i) *Transport Equations.* The equations for water and electrolyte transport were as follows.

Water Transport. The volume flux across a membrane is given by,

$$J_v = L_p(\Delta p - \Delta\pi) \tag{1a}$$

where L_p is the water permeability, Δp is the hydrostatic pressure difference and $\Delta\pi$ is the osmotic pressure difference,

$$\Delta\pi = RT\sum_i \Delta c_i \tag{1b}$$

where c_i is the concentration of solute i. R, T and Δ have their usual meanings.

Electrolyte transport.

1. *Single ion diffuse pathway* (*conductance*). Transmembrane flux of solute i (J_{di}) through a single ion diffusive pathway is described by the Goldman-Hodgkin-Katz equation:

$$J_{di} = -\frac{\omega_i z_i F\Delta E}{RT}\left\{\frac{c_i^1 - c_i^2\exp(z_i F\Delta E/RT)}{1-\exp(z_i F\Delta E/RT)}\right\} \tag{2}$$

where ω_i is the permeability coefficient of solute i, z_i is the valence of solute i, c_i^1 and c_i^2 are the concentrations of solute i in the two compartments separated by the membrane and ΔE is the electrical potential difference. R, T, and F have their usual meanings.

Unless otherwise specified, the model contained Cl^- and HCO_3^- diffusive pathways on the luminal membrane, and Na^+ and K^+ diffusive pathways on the basolateral membrane and in the paracellular junctional pathway. It should be noted that both Cl^- and HCO_3^- diffusive pathways on the luminal membrane might be underlied by the same anion channels (mainly CFTR- and Ca^{2+}-activated Cl^- channels). If Cl^- and HCO_3^- move through the same multi-ion channels [26], there

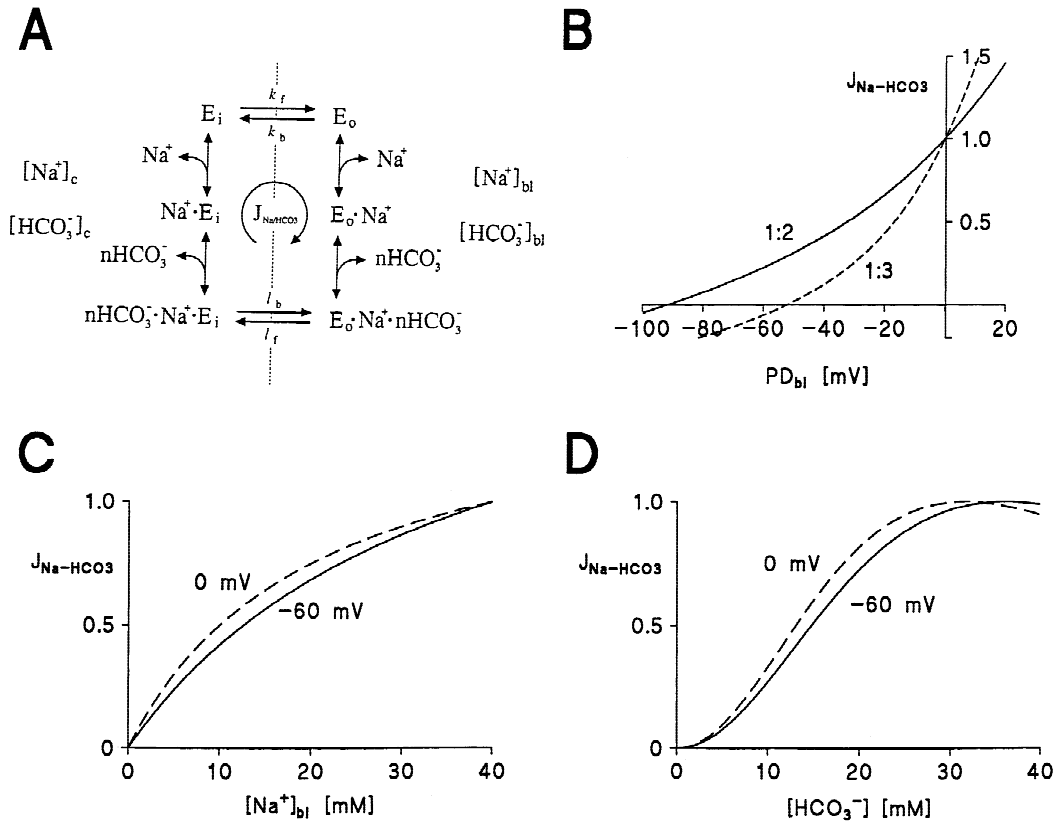

Fig. 2. Characteristics of the model Na^+-HCO_3^- cotransporter. (*A*) Kinetic model used to derive the turnover rates of the Na^+-HCO_3^- cotransporter (J_{NaHCO3}). (*B*) Plots of J_{NaHCO3} against PD_{bl}. $[Na^+]_c$ = 12.7 mM, $[Na^+]_{bl}$ = 146 mM, $[HCO_3^-]_c$ = 15.9 mM, $[HCO_3^-]_{bl}$ = 25 mM. The coupling ratio of HCO_3^- to Na^+ transport is (Solid line) 1:2 and (Dashed line) 1:3, respectively. (*C*) Effect of Na^+ on J_{NaHCO3}. $[Na^+]_c$ = 0 mM, $[HCO_3^-]_c$ = 21 mM, $[HCO_3^-]_{bl}$ = 21 mM. PD_{bl} = (Solid line) 0 mV and (Dashed line) −60 mV. The coupling ratio of HCO_3^- to Na^+ transport is 1:2. (*D*) Effect of HCO_3^- on J_{NaHCO3}. $[Na^+]_c$ = 0 mM, $[Na^+]_{bl}$ = 8 mM, PD_{bl} = (Solid line) 0 mV and (Dashed line) −60 mV. $[HCO_3^-]_c$ and $[HCO_3^-]_{bl}$ are changed symmetrically. The coupling ratio of HCO_3^- to Na^+ transport is 1:2. Values of model parameters (K_{cNa}, K_{cHCO3}, R_{lk}, n_{co}) are shown in Table 1. Values of $[Na^+]$ and $[HCO_3^-]$ used in Fig. 2*C* and *D* mimic the condition of the corresponding experiments in the literature [1].

might be a direct interaction between Cl^- flux and HCO_3^- flux. Indeed, it has recently been reported that extracellular $[HCO_3^-]$ reduces the whole cell Cl^- conductance in guinea-pig duct cells [31]. However, in contrast, current-voltage curves obtained from single CFTR Cl^- channels under some Cl^-/HCO_3^- bi-ionic conditions were well fitted by the sum of the Goldman equations for Cl^- and HCO_3^- [32]. Moreover, an anion channel that is different from CFTR and which has a Cl^-:HCO_3^- permeability ratio of 1:1 has been identified on CAPAN-1 cells, although its contribution to the luminal anion conductance and its regulation are still unknown [27]. Because of the uncertainty about the nature of the Cl^- and HCO_3^- diffusive pathways on the apical membrane of the duct cell, we have employed a combination of two single ion diffusive pathway formulations in our model (Eq. 2). By changing the permeability coefficients ($\omega_{Cl(l)}$ and $\omega_{HCO3(l)}$) of these luminal pathways we could easily alter the anion permeability characteristics of the luminal membrane. The basolateral Na^+ diffusive pathway (which may represent Na^+-coupled electrogenic transporters on the basolateral membrane [36]) was added so that the model accurately reproduced experimental data on the effects of $[K^+]_{bl}$ and K^+ channel blocker on PD_{bl} [28].

2. Antiporters. The model has Cl^-/HCO_3^- antiporters located on both luminal and basolateral membranes and Na^+/H^+ antiporters located on the basolateral membrane. The turnover rates of the Na^+/H^+ exchanger ($J_{Na/H}$), and the luminal and basolateral Cl^-/HCO_3^- antiporters ($J_{Cl/HCO3(l)}$ and $J_{Cl/HCO3(bl)}$) were expressed as previously described [36]. The dissociation constants for the antiporters (K_{Na}, K_H, K_{Cl} and K_{HCO3}, Table 1) were derived from published data [20, 21, 25, 35, 41, 42, 43].

3. Cotransporter. The model has an electrogenic Na^+-HCO_3^- cotransporter located on the basolateral membrane. Expressions for the turnover rate of this cotransporter were derived from a simplified (lumped) kinetics scheme including the 6 states shown in Fig. 2*A*. This scheme can quantitatively describe the kinetics of the Na^+-HCO_3^- cotransporter in renal proximal tubule cells [18].

We assumed: (i) that this cotransporter had single sites which bound a Na^+ ion and $nHCO_3^-$ ions with the sequential binding steps for the HCO_3^- ions being lumped together; (ii) that the cotransporter could only cross the membrane with either no ions bound or all ions bound; (iii) that the velocity constants at PD_{bl} = 0 mV outside to inside and inside to outside were the same for the cross-membrane step with (P_l) and without (P_k) carrying the ions; (iv) that the kinetic step between $E_o Na^+ nHCO_3^-$ and $nHCO_3 Na^+ E_i$ was voltage-independent but the step between E_o and E_i was voltage-dependent (carrying the net charge of $n-1$, $zL = n-1$); (v) that the dissociation constants (K_{cNa} and K_{cHCO3})

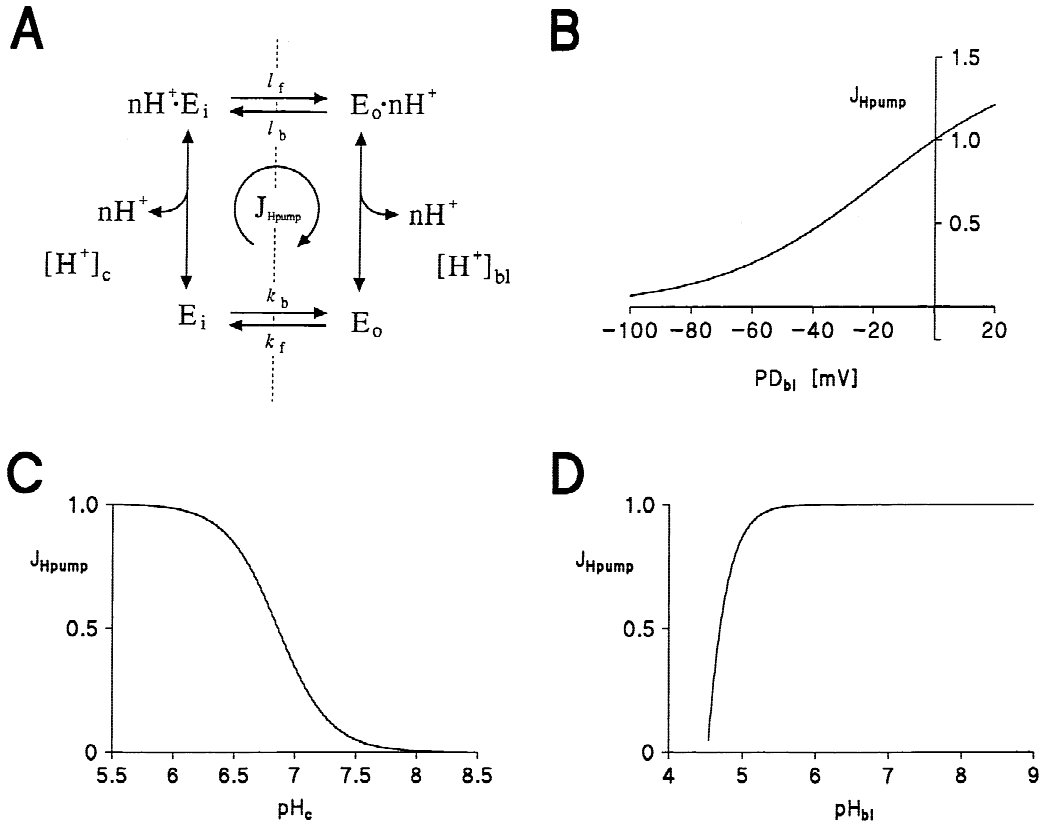

Fig. 3. Characteristics of the model H^+ pump. (*A*) Kinetic model used to derive the turnover rates of the H^+ pump (J_{Hpump}). (*B*) Voltage-dependence of J_{Hpump} (normalized to the value at 0 mV). pH_c = 7.2, pH_{bl} = 7.2. (*C*) Effect of intracellular pH (pH_c) on J_{Hpump} (normalized to the value at pH_c = 5.5). pH_{bl} = 7.2. PD_{bl} = −60 mV. (*D*) Effect of basolateral pH (pH_{bl}) on J_{Hpump} (normalized to the value at pH_{bl} = 9). pH_c = 7.2. PD_{bl} = −60 mV. Values of model parameters ($R_{lf/kc}/K_{Hpc}$, $R_{lb/kbl}/K_{Hpbl}$, n_{Hp}) used in Fig. 3*B–D* are shown in Table 1.

for each ion at the intracellular and extracellular faces of the membrane were the same. Therefore, the turnover rate of the Na^+-HCO_3^- cotransporter ($J_{Na\text{-}HCO3}$), can be expressed as follows (*see* Appendix A).

$$J_{Na\text{-}HCO3} = \frac{G_{Na\text{-}HCO3}\left\{\left(\frac{[Na^+]_{bl}[HCO_3^-]_{bl}^n}{K_{cNa}K_{cHCO3}^n}\right)\cdot\exp(-(1-n)\cdot F\cdot PD_{bl}/2RT) - \left(\frac{[Na^+]_c[HCO_3^-]_c^n}{K_{cNa}K_{cHCO3}^n}\right)\cdot\exp((1-n)\cdot F\cdot PD_{bl}/2RT)\right\}}{\left\{\exp((1-n)\cdot F\cdot PD_{bl}/2RT) + R_{l/k}\cdot\frac{[Na^+]_{bl}[HCO_3^-]_{bl}^n}{K_{cNa}K_{cHCO3}^n}\right\}\left(1+\frac{[Na^+]_c}{K_{cNa}}+\frac{[Na^+]_c[HCO_3^-]_c^n}{K_{cNa}K_{cHCO3}^n}\right) + \left\{\exp(-(1-n)\cdot F\cdot PD_{bl}/2RT) + R_{l/k}\cdot\frac{[Na^+]_c[HCO_3^-]_c^n}{K_{cNa}K_{cHCO3}^n}\right\}\left(1+\frac{[Na^+]_{bl}}{K_{cNa}}+\frac{[Na^+]_{bl}[HCO_3^-]_{bl}^n}{K_{cNa}K_{cHCO3}^n}\right)} \quad (3)$$

where $R_{l/k} = P_l/P_k$ are the velocity constant ratios of the cross-membrane steps with and without carrying the ions; $G_{Na\text{-}HCO3}$ is the permeability coefficient for the Na^+-HCO_3^- cotransporter.

The large value of $R_{l/k}$ (1×10^2, Table 1), which means that the voltage-dependent cross-membrane step between E_o and E_i is the rate-limiting step ($P_k << P_l$), is consistent with the experimental finding [18]. Values of K_{cNa} and K_{cHCO3} were determined to reproduce the apparent K_m values of ~10–15 mM for each ion (Fig. 2*C* and *D*), obtained from experimental data in the literature [1, 17, 18], and the necessity for accurate simulations of some experimental results (*see* Results and Discussion). We found that the voltage-dependency of $J_{Na/HCO3}$ was approximately linear over the physiological range of potentials (Fig. 2*B*), which is consistent with experimental data [18]. Overall, the data in Fig. 2 show that our model can accurately reproduce the basic characteristics of the Na^+-HCO_3^- cotransporter as described in the literature [1, 6, 17, 18, 34].

4. Na^+/K^+ pump. The turnover rate of the Na^+/K^+ pump ($J_{NaKpump}$) was expressed as previously described [19, 36]. The saturation constants were K_{pNa} = 25 mM for intracellular Na^+, and K_{pK} = 1.4 mM for extracellular K^+. The apparent reversal potential (E_{rev}) was set to −200 mV in order to reproduce an accurate voltage-dependence of $J_{NaKpump}$ over the physiological range of PD_{bl} [2, 33, 45].

5. H^+ pump. The model has an electrogenic (vacuolar-type) H^+ pump located on the basolateral membrane. Expressions for the turnover rate of this pump were derived from a simplified (lumped) kinetics scheme including 4 states shown in Fig. 3*A*. We assumed: (i) that the pump has a single site which bound nH^+ ions; (ii) that the transporter could only cross the membrane with no ions bound or nH^+ ions bound;

(iii) that the kinetic step between nH^+E_i and E_onH^+ ('ATP' step) was voltage-dependent (carrying a net charge of $+n$) and that the velocity constant at $PD_{bl} = 0$ mV for transport from inside to outside (P_{lf}) is larger than from outside to inside (P_{lb}), which characterizes the process as primary active transport; (iv) that the kinetic step between E_o and E_i ('non-ATP' step) was voltage-independent and that the velocity constants at $PD_{bl} = 0$ mV for transport from outside to inside and from inside to outside were the same (P_k). Therefore, the turnover rate of the H^+ pump (J_{Hpump}), can be expressed as follows (*see* Appendix A).

$$J_{Hpump} = \frac{G_{Hpump}\left\{R_{lf/k}\left(\frac{[H^+]_c^n}{K_{Hpc}}\right)\exp(n \cdot F \cdot PD_{bl}/2RT) - R_{lb/k}\left(\frac{[H^+]_{bl}^n}{K_{Hpbl}}\right)\exp(-n \cdot F \cdot PD_{bl}/2RT)\right\}}{R_{lf/k}\left(\frac{[H^+]_c^n}{K_{Hpc}}\right)\exp(n \cdot F \cdot PD_{bl}/2RT) + R_{lb/k}\left(\frac{[H^+]_{bl}^n}{K_{Hpbl}}\right)\exp(-n \cdot F \cdot PD_{bl}/2RT) + 2} \quad (4)$$

where $R_{lf/k} = P_{lf}/P_k$ and $R_{lb/k} = P_{lb}/P_k$ are the velocity constant ratios of the forward and backward reactions of the 'ATP' step and the 'non-ATP' step, respectively; K_{Hpc} and K_{Hpbl} are dissociation constants for H^+ at the cytoplasmic and basolateral faces of the membrane, respectively; G_{Hpump} is the permeability coefficient for the H^+ pump. Note that J_{Hpump} is determined by values of $R_{lf/k}/K_{Hpc}$ and $R_{lb/k}/K_{Hpbl}$ in addition to n and G_{Hpump}.

Davies et al. [8] suggested that the stoichiometry of H^+:ATP in a vacuolar H^+ pump might be variable (1:1 or 3:1). However, the same group [8] also showed that a 2-state simplified scheme with H^+:ATP = 2:1, which is essentially identical to our H^+ pump model, can reproduce accurately the current-voltage curve of the vacuolar H^+ pump, except for the weak sensitivity of the zero-current voltage to the transmembrane pH gradient.

The voltage-dependency of J_{Hpump} is a superlinear curve approaching saturation at more depolarized potentials than the physiological range (Fig. 3*B*), which is basically consistent with experimental data [8, 10]. Note that the physiological range of PD_{bl} is far depolarized from the pump reversal potential (−225 mV with pH_c, pH_{bl} = 7.2; −237 mV with pH_c and pH_{bl} = 7.2 and 7.4 respectively), so that J_{Hpump} should be accurately reproduced by the model. Figure 3*C* shows that the pH_c-dependency of J_{Hpump} is sigmoidal reaching a maximal value as pH_c is decreased. J_{Hpump} increases sharply at pH_c values lower than the physiological range, which means that the model H^+ pump is activated when the cell is acid overloaded. In contrast, changes in extracellular pH (pH_{bl}) over the physiological range have no effect on J_{Hpump} (Fig. 3*D*). Although the characteristics of the vacuolar-type H^+ pump in epithelia including pancreatic duct cells are not known in detail, the accurate reproduction of experimental data relating to the contribution of the H^+-pump to H^+ extrusion across the basolateral membrane (Fig. 4*B*), suggests that the assumptions we make are appropriate.

(ii) Buffering Equations. The model contains a HCO_3^-/CO_2 buffering system and an intrinsic non-CO_2 buffering system which we have previously described [36]. Intracellular H^+ was buffered by both of these systems. In the fluid-secreting model, the HCO_3^-/CO_2 buffering system is also present in the luminal compartment. The apparent acid dissociation constant of the HCO_3^-/CO_2 buffering system, K_{CO2}, was set at 24.9×10^{-12} M^2/mmHg. The 'apparent' acid dissociation constant of the intrinsic non-CO_2 buffering system, K_{HB}, and the total intrinsic buffer ($[HB]+[B^-]$), B_{total}, were set at 0.04 mM and 6 M, respectively. These values for intrinsic buffer capacity may seem unrealistically high. However, with these parameter values, the model intrinsic buffering system [36] can accurately reproduce the experimentally measured intrinsic buffering capacity of pancreatic duct cells (which might consist of many different buffering species with widely different concentrations and dissociation constants), over a wide pH range between ~6.6 and ~8.0 [43]. Note that the intrinsic buffering system of the model is required to reproduce the buffering capacity over a wide pH range because some simulations were performed under conditions of strong cellular acidification or alkalinization (e.g., Fig. 4). We found that a buffering system with 'realistic' parameters (e.g., $K_{HB} = 10^{-7}$ M and B_{total} = 40 mM) cannot reproduce the experimentally measured buffering capacity, especially in the acidification range (*data not shown*).

Fluid Compositions

The compositions of the bathing solutions (a HCO_3^-/CO_2-buffered solution and a HCO_3^-/CO_2-free, HEPES-buffered solution) used in the simulations have been previously described [36]. Note that the HEPES-buffered solution contains 0.2 mM HCO_3^- derived from CO_2 in the air (0.04%) [36]. To stimulate either Na^+-free or Cl^--free conditions these ions were replaced by an impermeable solute, X. To simulate the effects of increasing luminal $[HCO_3^-]$, luminal Cl^- was replaced by HCO_3^-.

The Two Versions of the Model

We developed two different versions of the computer model: a non-fluid-secreting version and a fluid-secreting version, and used each version as detailed below.

(i) Nonfluid-secreting model. In this model, initial values of the volumes of both luminal and basolateral compartments were all set to large values (1×10^{80} ml/cm^2 epithelium). Therefore, changes in the volumes and solute concentrations of these luminal and basolateral compartments were negligible during simulations [36]. Because we can keep luminal and basolateral solute concentrations constant at a chosen value, we used this version of the model: (i) for investigating the basic ion transport characteristics of the model cell when bathed in solutions of selected composition (e.g., symmetrical HCO_3^-/CO_2-buffered solutions or HCO_3^-/CO_2-free, HEPES-buffered, solutions) allowing comparison of the model's characteristics with experimental data obtained from double-perfused ducts [28, 29, 30, 46] (e.g., Figs. 4 and 5), and (ii) for simulating ion transport against a luminal solution containing a chosen (high) concentration of HCO_3^- (e.g., Fig. 7).

(ii) Fluid-secreting model. We also developed a version of the simulation model in which a fluid is 'actually' secreted into the lumen. In this model, initial luminal compartment volume was set to a small value (1×10^{-3} ml/cm^2 epithelium) and the luminal solution was removed from the luminal compartment at the same rate as the fluid was secreted. Therefore, the volume of the luminal compartment remained constant at the initial small value and the contents of the luminal compartment were changed quickly dependent on the composition of the fluid secreted by the model cell. The model cell transports ions into the luminal compartment, which increases the osmolarity of the luminal solution (e.g., Tables 4 and 7), and the water is driven into the lumen according to the osmotic pressure differences (Eqs. 1*ab*). We used the fluid-secreting model to investigate the rate and maximum HCO_3^- concentration of the fluid secreted by the pancreatic duct cell (e.g., Figs. 6 and 8). In both types of model, initial values of the static pressure and compliance of all compartments were set to 1 atm and the large value of 1×10^{80} l/atm, respectively. Therefore, static pressure differences between compartments were negligible.

Numerical Solution

The model variables were computed in the way we have previously described [36]. The net fluxes of solute *i* across a membrane (pathway)

m ($J_{i(m)}$) were calculated as the sum of all fluxes of solute i via all transport elements existing on the membrane [36]. The total fluxes of water ($Flw_{v(k)}$), solute ($Flw_{i(k)}$) and electrical charge movement ($Flw_{e(k)}$) into the compartment k were calculated from $J_{i(m)}$ in the same way as we have previously described [36]. The model variables at time $t + dt$ before significant buffering had taken place, $Vol_{(k),t+dt}$, $p_{(k),t+dt}$, $[i]_{k,t+dt}$ and $E_{(k),t+dt}$, were calculated from the equations below (5*a*–5*d*) using Euler's method.

$$Vol_{(k),t+dt} = Vol_{(k),t} + Flw_{v(k)} \cdot dt \tag{5a}$$

$$p_{(k),t+dt} = p_{(k),t} + Flw_{v(k)} \cdot dt/C_{p(k)} \tag{5b}$$

$$[i]_{k,t+dt} = ([i]_{k,t} \cdot Vol_{(k),t} + Flw_{i(k)} \cdot dt)/Vol_{(k),t+dt} \tag{5c}$$

$$E_{(k),t+dt} = E_{(k),t} + Flw_{e(k)} \cdot dt/C_{e(k)} \tag{5d}$$

where dt is the integration interval; $C_{p(k)}$ is the compliance of compartment k; and $C_{e(k)}$ is the electrical capacitance of compartment k.

For calculating the potential, we employed a conventional method with a conceptual capacitor corresponding to each compartment (Eq. 5*d*, *see* Appendix B for detail).

In the fluid-secreting model, luminal solution is removed from the luminal compartment at the same rate as fluid is secreted into the compartment by the model cell, J_{vfld}.

$$Vol_{(l),t+dt} = Vol'_{(l),t+dt} - J_{vfld} \cdot dt\ (= Vol_{(l),t}) \tag{6}$$

where $Vol'_{(l),t+td}$ was the volume of luminal compartment at time $t + dt$ before the reduction of the volume. Note that J_{vfld} is equal to $Flw_{v(l)}$ in the fluid secreting model.

Concentrations of the weak base (B^-), and its conjugate weak acid (HB) in the (intracellular) intrinsic buffering system, [B^-] and [HB], were also calculated by Eq. (5*c*) with $Flw_{i(c)} = 0$. Of the model variables at time $t + dt$, those concerned with the buffering systems, $[H^+]_{c,t+dt}$, $[HCO_3^-]_{c,t+dt}$, $[B^-]_{c,t+dt}$ and $[HB]_{c,t+dt}$ (also $[H^+]_{l,t+dt}$ and $[HCO_3^-]_{l,t+dt}$ in the fluid-secreting model) were sequentially modified by the buffering equations, according to the method we have previously described [36]. Buffering did not change the other variables.

Note that the model cell was assumed to have a nonfluid volume component (0.4 μl/cm^2 epithelium: 40% of the initial volume). Therefore, the cell volume, Vol_{cell}, is calculated as the sum of $Vol_{(c)}$ and the nonfluid component [36].

The computer programs calculated the model equations with dt = 2 msec, using the double precision data type. Decreasing dt 10-fold (dt = 0.2 msec) had no effect on the calculated time courses of the model variables.

Simulating Experimental Data

To simulate experimental data for checking the accuracy of our model, we mainly used the nonfluid-secreting version and changed the model parameters, for example, $[i]_{l,bl}$, ω_i, $G_{Na/H}$ and $G_{Cl/HCO3}$, etc., as appropriate according to the experimental conditions.

Short-Circuit Current

The model was usually run under open-circuit conditions. However, for measuring the short-circuit current (I_{sc}) the model was occasionally run under short-circuit conditions. To simulate the short-circuit condition, we applied a current (I_{sc}) from the basolateral to the luminal compartment at the end of the dt interval (*see* Appendix B for detail).

$$I_{sc} = \frac{Flw_{e(bl)} - Flw_{e(l)}}{2} \tag{7}$$

After changing the moel from the open-circuit condition to the short-circuit condition, the model variables including I_{sc} were changing at every dt interval until a steady state was reached. Therefore, we utilized the value of I_{sc} soon (1 sec) after changing the experimental condition [28].

Voltage Divider Ratio

The voltage divider ratio (VDR) was calculated using the following equation:

$$VDR = \frac{\left[\begin{array}{l}\displaystyle\sum_i \frac{\Delta(z_i \cdot F \cdot J_{di(bl)})}{\Delta PD_{bl}} + \frac{\Delta\{(1 - n_{co}) \cdot F \cdot J_{NaHCO3}\}}{\Delta PD_{bl}} \\ \quad + \dfrac{\Delta(n_{Hp} \cdot F \cdot J_{Hpump})}{\Delta PD_{bl}} \\ \quad + G_{pump}\left(\dfrac{[Na^+]_c}{[Na^+]_c + K_{pNa}}\right)^3\left(\dfrac{[K^+]_{bl}}{[K^+]_{bl} + K_{pK}}\right)^2\end{array}\right]}{\displaystyle\sum_i \frac{\Delta(z_i \cdot F \cdot J_{di(l)})}{\Delta PD_l}} \tag{8}$$

where $\Delta(z_i \cdot F \cdot J_{di(bl)})/\Delta PD_{bl}$, $\Delta\{(1 - n_{co}) \cdot F \cdot J_{NaHCO3}\}/\Delta PD_{bl}$ and $\Delta(n_{Hp} \cdot F \cdot J_{Hpump})/\Delta PD_{bl}$ were calculated with ΔPD_{bl} = 1 mV, and $\Delta(z_i \cdot F \cdot J_{di(l)}/\Delta PD_l$ was calculated with ΔPD_l = 10 mV and 1 mV in resting and stimulated conditions, respectively, according to th method of the experiment to be reproduced [28]. Note that values of the parameters and variables per cm^2 epithelium (not per cm^2 membrane) are used for calculating Eq. (8).

Fluid Secretion

In the fluid-secreting model, we calculated the rate of fluid secretion (J_{vfld}) and the effective HCO_3^- concentration of the secreted fluid ($[HCO_3^-]_{fld}$) as shown below:

$$J_{vfld} = Flw_{v(l)} \tag{9}$$

$$[HCO_3^-]_{fld} = \frac{Flw_{HCO3(l)}}{Flw_{v(l)}} \tag{10}$$

Note that $[HCO_3^-]_{fld}$ is a conceptual variable and that the value of $[HCO_3^-]_{fld}$ can become negative during transient states in which net HCO_3^- influx across the luminal membrane occurs (e.g., Fig. 6*A*).

In the nonfluid-secreting model, anion secretion (Cl^- and HCO_3^-) is driven directly whereas cation (Na^+ and K^+) secretion is driven by the potential difference across the epithelium. However, there is no net volume flow across the model epithelium because changes in solute concentrations and static pressures of the luminal and basolateral compartments are assumed to be negligible. Therefore, we assumed that there was a virtual isotonic fluid secretion driven by anion transport in the model cell. In this model, we defined the rate of (virtual) fluid secretion (J_{vfld}) and the effective HCO_3^- concentration in the secreted fluid ($[HCO_3^-]_{fld}$) as shown below:

$$J_{vfld} = \frac{\displaystyle\sum_i Flw_{i(l)}}{c_{total}} \tag{11}$$

$$[HCO_3^-]_{fld} = \frac{c_{total} \cdot Flw_{HCO3(l)}}{\sum_i Flw_{i(l)}} \quad (12)$$

where c_{total} is the total concentration of all solutes contained in the bathing solutions (315.5 mM). Compared with the fluid-secreting model under the same condition, the calculated value of J_{vfld} is overestimated by a maximum of 8.5% and $[HCO_3^-]_{fld}$ is underestimated by a maximum of 1.5%. Therefore these conceptual variables are useful indicators for expressing the characteristics of the nonfluid secreting model.

Parameter Selection

Values for the membrane and transport parameters that we employed are given in Table 1. Luminal, basolateral and paracellular membrane areas, and the cell volume of 1 μl/cm^2 epithelium were calculated from morphological data [3]. Water permeabilities of the luminal ($Lp_{(l)}$) and basolateral ($Lp_{(bl)}$) membranes were set at 1×10^{-5} cm/sec/atm [38, 39, 40]. *Lp* of the paracellular junctional pathway ($Lp_{(j)}$) was assumed to be 1×10^{-3} cm/sec/atm. With $Lp_{(j)}$ of 1×10^{-3} cm/sec/atm, fluid secretion by the (fluid-secreting) model can be regarded as an isotonic secretion because the osmolarity of the secreted fluid is less than 4% higher than that of the bathing solution (*see* Tables 4 and 7). Under this condition, the contribution of the transcellular route and the paracellular route to the total transepithelial water flow is approximately 1:1. Even assuming $Lp_{(j)}$ of 0 cm/sec/atm, the models still secreted a near-isotonic fluid whose osmolarity was only 7.4% higher than the bathing solution. All reflection coefficients of membrane to solutes (σ) were assumed at 1. This assumption might not be accurate for the paracellular pathway, in which water and solutes flow in a same diffusive pathway and interact with each other. However, variations of paracellular σ as well as in $Lp_{(j)}$ did not lead us to change our conclusions (*data not shown*).

The resting permeability of the luminal membrane of Cl^- ($\omega_{Cl(l)}$), and of the basolateral membrane to K^+ ($\omega_{K(bl)}$) and Na^+ ($\omega_{Na(bl)}$) were set to reproduce the voltage divider ratio (VDR) of ~8 determined from experiments on microperfused ducts [28, 29, 30], and experimental data on the effects of step changes in basolateral K^+ concentration [28] and basolateral K^+ conductance on PD_{bl} [36] (Table 1). The luminal Cl^- conductance is provided by CFTR and Ca^{2+}-activated Cl^- channels. It is known that CFTR has a significant permeability to HCO_3^- [14], and the same is likely to be true for the Ca^{2+}-activated Cl^- channels. From experimental data [14], the luminal membrane HCO_3^- permeability coefficient, $\omega_{HCO3(l)}$ was set to be 6.2×10^{-10} cm/sec, which means a permeability ratio of $Cl^-:HCO_3^- = 5:1$.

We assumed that the paracellular pathway is permeable to Na^+ and K^+ but not to Cl^- and HCO_3^-. Experimental data for paracellular ionic permeability in pancreatic ducts are not available, therefore, it is possible that the paracellular pathway is permeable to anions. Adding paracellular Cl^- ($\omega_{Cl(j)}$) and HCO_3^- ($\omega_{HCO3(j)}$) permeabilities caused Cl^- influx into, and HCO_3^- efflux out of, the luminal compartment and decreased J_{vfld} and $[HCO_3^-]_{fld}$. Thus a paracellular nonselective anion conductance decreased the ability of the model epithelium to secrete a HCO_3^--rich fluid. With a small nonselective anion permeability in the paracellular pathway ($\omega_{Cl(j)}$ and $\omega_{HCO3(j)}$ of higher than 6.9×10^{-8} cm/sec, that is 1.9% of the cation permeability), the high bicarbonate model failed to secrete a fluid of over 140 mM $[HCO_3^-]$ even after complete removal of the luminal Cl^- diffusive pathway and the luminal Cl^-/HCO_3^- antiporter (i.e., decreasing $\omega_{Cl(l)}$ and $G_{Cl/HCO3(l)}$ to 0) (*data not shown*). Therefore, it is unlikely that the paracellular pathway in pancreatic ducts could have a significant anion permeability.

The permeability coefficient for the Na^+/K^+ pump ($G_{NaKpump}$) was determined to reproduce the short-circuit current (I_{sc}) of ~20 μA/cm^2 observed in microperfused ducts [28], with reference to the intracellular Na^+ concentration of 12 mM [23] (*see* Table 1).

The permeability coefficients for the H^+/HCO_3^- transporters ($G_{Na/H}$, $G_{Cl/HCO3(l)}$, $G_{Cl/HCO3(bl)}$, $G_{Na/HCO3}$ and G_{Hpump}) were all determined from the literature and the necessity for accurate simulations of experimental data (*see* Results and Discussion for details).

Results and Discussion

Modelling the Effect of Basolateral Cl^-/HCO_3^- Antiporters, Na^+-HCO_3^- Cotransporters, and H^+ Pumps in the Computer Model

Our new computer model of the pancreatic duct cell contains Cl^-/HCO_3^- antiporters, Na^+-HCO_3^- cotransporters, and H^+ pumps on the basolateral membrane. In this section, we model the effect of altering the activity of these transport elements on various duct cell parameters and compare these data with experimental results.

Cl^-/HCO_3^- Antiporter

In our previous model of the duct cell [36], Cl^-/HCO_3^- antiporters were assumed to be located only in the luminal membrane. However, Zhao et al. [46] reported that in microperfused rat ducts, Cl^-/HCO_3^- exchanger activity could be detected on both the luminal and basolateral cell membranes. By mimicking the experimental data of Zhao et al. [46] (i.e, simulating the change in pH_c following removal of Cl^- from either the basolateral or luminal solutions), we estimated the antiporter distribution ratio (ADR) between the two membranes.

Figure 4*A* shows how changes in luminal and basolateral Cl^- concentration ($[Cl^-]_l$ and $[Cl^-]_{bl}$, respectively) affect pH_c with three different ADRs (4:1, 3:2 and 2:3). The basolateral Cl^--free condition (0.1 mM Cl^-) caused an alkalinization of pH_c, and the subsequent removal of luminal Cl^- caused a further alkalinization to around 7.6. The return of $[Cl^-]_{bl}$ to 125 mM initiated a partial recovery of pH_c, and the subsequent return of $[Cl^-]_l$ to 125 mM caused a complete recovery of pH_c to the control value of 7.2. Note that the magnitude of the pH_c changes in response to basolateral and luminal Cl^- removal depend on the ADR (Fig. 4*A*). Zhao et al. [46] reported that removal of either basolateral or luminal Cl^- had about the same effect on pH_c in microperfused ducts. Therefore, the ADR was set at 3:2 in our model on the basis of the data shown in Fig. 4*A*.

H^+ Pump

It was reported that pancreatic duct cells in pig and rat possess a Na^+-independent, vacuolar-type H^+ pump probably on the basolateral membrane [43, 46] (Fig. 1). Figure 4*B* shows how changes in luminal and basolateral

Table 1. Values of the membrane and transport parameters used in the model

	Luminal	Basolateral	Paracellular
A (cm^2)	1	14.3	0.01
L_p (cm/sec/atm)	1×10^{-5}	1×10^{-5}	1×10^{-3}
ω_i (cm/sec)			
Na^+	0	1.8×10^{-10}	3.6×10^{-6}
K^+	0	3×10^{-9}	3.6×10^{-6}
Cl^-	3.1×10^{-9} , 3×10^{-9} #	0	0
HCO_3^-	6.2×10^{-10}, 1.2×10^{-9} #	0	0
H^+	0	0	0
Na^+/K^+ pump			
$G_{NaKpump}$ (mol/V/sec/cm^2)		3×10^{-7}	
$E_{NaKprev}$ (mV)		−200	
K_{NaKpNa} (mM)		25	
K_{NaKpK} (mM)		1.4	
Na^+/H^+ antiporter			
$G_{Na/H}$ (mol/sec/cm^2)		2.5×10^{-10}	
K_{Na} (mM)		100	
K_H (mM)		5×10^{-4}	
Cl^-/HCO_3^- antiporter			
$G_{Cl/HCO3(l)}$ (mol/sec/cm^2)		7.2×10^{-9}, 1.08×10^{-8} #	
$G_{Cl/HCO3(bl)}$ (mol/sec/cm^2)		4.8×10^{-9}, 1.2×10^{-9} #	
K_{Cl} (mM)		10	
K_{HCO3} (mM)		1	
Na^+-HCO_3^- cotransporter			
$G_{Na/HCO3}$ (mol/sec/cm^2)		1.5×10^{-9}, 1×10^{-9} #	
K_{cNa} (mM)		500	
K_{cHCO3} (mM)		30	
R_{lk}		100	
n_{co}		2	
zL		1	
H^+ pump			
G_{Hpump} (mol/sec/cm^2)		1×10^{-11} (CO_2/HCO_3^--buffered) 0(HEPES-buffered)	
$R_{lf/k}/K_{Hpc}$ (/M^{nHp})		1×10^{15}	
$R_{lb/k}/K_{Hpbl}$ (/M^{nHp})		5×10^{7}	
n_{Hp}		2	

The permeabilities (L_p, ω_i, G_{pump}, $G_{Na/H}$, $G_{Na/HCO3}$ and G_{Hpump}) are values per 1 cm^2 membrane. $G_{Cl/HCO3(l)}$ and $G_{Cl/HCO3(bl)}$ are values per 1 cm^2 epithelium. #: high bicarbonate model.

Na^+ concentration, and the permeability coefficient for the H^+ pump (G_{Hpump}), affect pH_c in our computer model. When the luminal and basolateral compartments are Na^+-free, the Na^+/H^+ exchanger and the Na^+-HCO_3^- cotransporter do not carry H^+ or HCO_3^- significantly and pH_c is decreased from 7.2 to 6.7 (Fig. 4*B*). In this condition, H^+ is pumped out by the H^+ pump, and the H^+ pumping rate is equal to the HCO_3^- efflux rate via the Cl^-/HCO_3^- antiporters and the luminal HCO_3^- conductance. Complete inhibition of the H^+ pump ($G_{Hpump} = 0$) induced a further acidification of pH_c from 6.7 to 6.4 which was fully reversed following reactivation of the pump (Fig. 4*B*). From the experimental data reported by Zhao et al. [46], pH_c under Na^+-free conditions, with and without the H^+ pump inhibitor, bafilomycin, seemed to be 6.3–6.6 and 6.7–6.8, respectively. This agreement between experimental and simulation results supports the idea that the G_{Hpump} was appropriately estimated as 1×10^{-11} mol/sec/cm^2.

Na^+-HCO_3^- Cotransporter

Pancreatic duct cells of the rat and guinea pig possess an Na^+-HCO_3^- cotransporter on their basolateral membrane [46, 23]. We employed the Na^+:HCO_3^- coupling ratio of 1:2 ($n_{co} = 2$) [34] because the cotransporter would work as an acid extruder [6, 23]. Figure 4*C* and *D* show that the change in pH_c induced by symmetrical Cl^--free conditions (ΔpH_c) was strongly dependent on $G_{Na\text{-}HCO3}$. This occurs because the Na^+-HCO_3^- cotransporter is the only acid loader under these conditions. From the steady-state ΔpH_c observed experimentally in symmetrical Cl^--free conditions (about 0.4, [46]), the $G_{Na\text{-}HCO3}$ of unstimulated duct cells was estimated as 1.5×10^{-9} mol/sec/cm^2 (Fig. 4*D*).

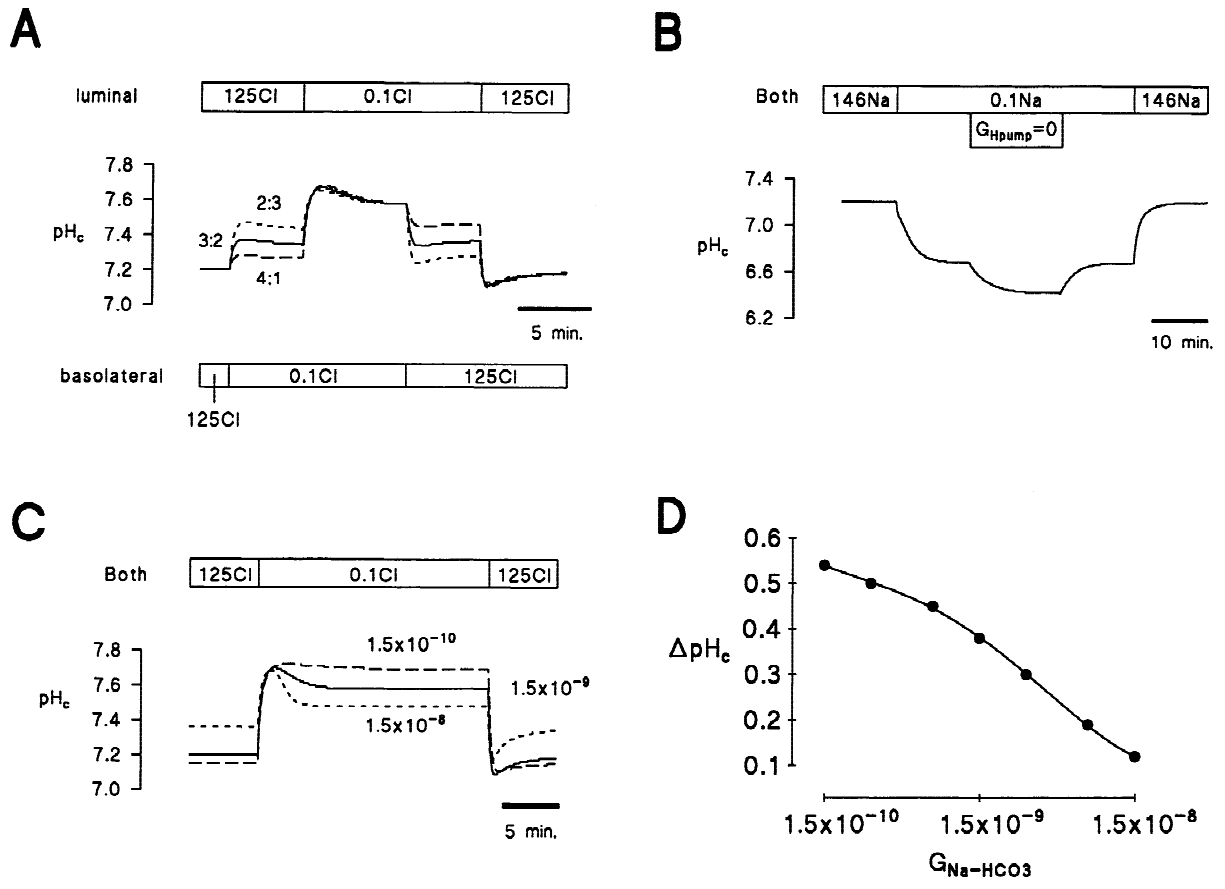

Fig. 4. Determination of permeability coefficients of H^+/HCO_3^- transporters in the model. (*A*) Cl^-/HCO_3^- antiporters: simulated results for the effects of reducing the luminal and/or basolateral Cl^- concentrations ($[Cl^-]_l$, $[Cl^-]_{bl}$) on intracellular pH (pH_c). The luminal:basolateral Cl^-/HCO_3^- antiporter distribution ratios (ADR) are (short dashed line) 2:3, (solid line) 3:2 and (long dashed line) 4:1. Note that ADR represents the ratio of Cl^-/HCO_3^- exchange (Cl^- influx and HCO_3^- efflux) activities on the luminal and basolateral membranes. The model duct was bathed with symmetrical HCO_3^-/CO_2-buffered solutions and Cl^- was replaced by an impermeant anion. (*B*) H^+ pump: simulated results for the effects of luminal and basolateral Na^+ concentration and the permeability coefficient of H^+ pump (G_{Hpump}) on pH_c in the computer model. Bathed with symmetrical HCO_3^-/CO_2-buffered solutions. Na^+ on both luminal and basolateral sides was replaced by an impermeant cation. (*C* and *D*) Na^+-HCO_3^- cotransporter: (*C*) Simulated results for the effects of symmetrical Cl^--free solutions on pH_c with different $G_{Na\text{-}HCO3}$ values in the model. The coupling ratio of the Na^+-HCO_3^- cotransporter is 1:2. Values of $G_{Na\text{-}HCO3}$ are (long dashed line) 1.5×10^{-10}, (solid line) 1.5×10^{-9} and (short dashed line) 1.5×10^{-8}. Bathed with symmetrical HCO_3^-/CO_2-buffered solutions. Cl^- on both luminal and basolateral sides was replaced by an impermeant anion. (*D*) Summary of the effects of $G_{Na\text{-}HCO3}$ on pH_c under symmetrical Cl^--free conditions. ΔpH_c is defined as pH_c in Cl^--free condition minus pH_c in the control condition (*see* Fig. 4*C*). Data were recorded 20 min. after the step change in $[Cl^-]$.

Modelling the Resting and Stimulated Duct Cell

Using the transport equations described above, we have updated the simulation program to include all the transport elements shown in Fig. 1. We used the nonfluid-secreting model for checking the basic characteristics of ion transport and the fluid secreting model for investigating HCO_3^--rich fluid secretion (*see* Materials and Methods).

Basic Characteristics of Ion Transport

Resting Cell. The model remained in a steady state at rest. Steady-state values for the variables in the model are shown in Table 2. Steady-state fluxes and turnover rates under each condition are given in Table 3.

Several of the steady-state model variables compare well with values reported in the literature. For instance, Table 2 shows that, bathed with symmetrical CO_2/HCO_3^--free solutions, the basolateral membrane potential (PD_{bl}), the transepithelial potential (PD_{te}), the voltage divider ratio (VDR), the transepithelial resistance (R_{te}), and the equivalent short-circuit current (I_{sc}) were all similar to the values measured in microperfused ducts [28, 29, 30]. Moreover, intracellular pH (pH_c), was about 7.2 when the cells were bathed in a CO_2/HCO_3^--buffered solution which is similar to the measured value in the duct cell [41, 46] (Table 2). Table 2 also shows

Table 2. Values of model variables in resting and stimulated steady states of the nonfluid secretion model

Solutions	Model			Experimental data			
	HEPES	HCO_3^-/CO_2		HEPES	HCO_3^-/CO_2		
Condition	Resting	Resting	Stimulated	Resting	Resting	Stimulated	[ref.]
$[Na^+]_c$ (mM)	10.4	10.9	12.0	13	12	17	[22*]
$[K^+]_c$ (mM)	123.3	128.2	120.5	N/A	N/A	N/A	
$[Cl^-]_c$ (mM)	37.5	58.5	28.8	N/A	N/A	N/A	
$[HCO_3^-]_c$ (mM)	0.2	15.7	15.7	N/A	N/A	N/A	
$[X]_c$ (mM)	144.1	102.2	138.5	N/A	N/A	N/A	
pH_c	7.37	7.20	7.20	7.36	7.17	N/A	[46]
				7.35–7.54	7.28–7.42	−0.02ΔpH	[22*, 10]
PD_{bl} (mV)	−62.5	−62.0	−54.2	−63	N/A	N/A	[27]
PD_{te} (mV)	−0.9	−1.8	−6.6	−0.8	N/A	N/A	[27]
VDR	8.2	6.8	0.6	8.2	17*	0.8*	[29]
R_{te} (Ωcm^2)	49.4	49.0	41.3	50–80	~50*	~40*	[27, 29]
I_{sc} ($\mu A/cm^2$)	17.8	37.5	157.9	26	N/A	N/A	[27]
Vol_{cell} ($\mu l/cm^2$)	1.0	1.25	1.02	N/A	~1	N/A	[3]

Bathed on both the luminal and basolateral sides with either a HCO_3^-/CO_2-free, HEPES-buffered, solution or a HCO_3^-/CO_2-buffered solution. Experimental data were obtained from rat [3, 27, 29, 46] and guinea pig [22, 10].
Note that some experimental data (*) were not obtained under symmetrical double perfused conditions.
N/A = data not available. The stimulation is mimicked by $\omega_{Cl,HCO3(l)}$: ×20 ($\omega_{Cl(l)} = 6.2 \times 10^{-8}$ cm/sec, $\omega_{HCO3(l)} = 1.24 \times 10^{-8}$ cm/sec) and $G_{Na\text{-}HCO3}$: ×11 ($= 1.65 \times 10^{-8}$ mol/sec/cm^2).

Table 3. Steady-state ion fluxes and transporter turnover rates (nmol/min/cm^2 epithelium) in the nonfluid secreting model under the resting and stimulated conditions

Solution	HEPES	HCO_3^-/CO_2	
Condition	Resting	Resting	Stimulated
$J_{HCO3(l)}$	6.5	14.0	55.5
$J_{Cl(l)}$	4.3	8.5	24.7
$J_{dHCO3(l)}$	0.0	1.2	18.4
$J_{dCl(l)}$	10.7	21.3	61.9
$J_{Cl/HCO3(l)}$	6.4	12.8	37.1
$J_{Cl/HCO3(bl)}$	4.3	8.5	24.7
$J_{Na/H}$	10.8	15.2	14.7
$J_{Na\text{-}HCO3}$	0.0	4.5	61.9
J_{Hpump}	0.0	2.8	3.6
$J_{dNa(bl)}$	58.0	57.7	52.1
$J_{dK(bl)}$	−45.8	−50.1	−65.2
$J_{NaKpump}$	22.9	25.0	32.6
$J_{Na(j)}$	10.4	21.8	77.6
$J_{K(j)}$	0.4	0.7	2.7

Turnover rates of H^+/HCO_3^- transporters are converted into their H^+/HCO_3^- transport rates. Bathed on both the luminal and basolateral sides with either a HCO_3^-/CO_2-free, HEPES-buffered, solution or a HCO_3^-/CO_2-buffered solution. The stimulation is mimicked by $\omega_{Cl,HCO3(l)}$: ×20 ($\omega_{Cl(l)} = 6.2 \times 10^{-8}$ cm/sec, $\omega_{HCO3(l)} = 1.24 \times 10^{-8}$ cm/sec) and $G_{Na\text{-}HCO3}$: ×11 ($= 1.65 \times 10^{-8}$ mol/sec/cm^2).

that on switching from a CO_2/HCO_3^--buffered solution to a HEPES-buffered solution, pH_c alkalinized by about 0.2 units which is consistent with experimental findings [41, 46, 23]. Note that even in the presence of HEPES-buffered solutions, a small but significant HCO_3^- flux occurs via the Cl^-/HCO_3^- antiporters because of the 0.2 mM HCO_3^-, derived from atmospheric CO_2, contained in these solutions (Table 3). In the resting condition, bathed with symmetrical CO_2/HCO_3^--buffered solutions, more than 90% of the secreted HCO_3^- is carried via the luminal Cl^-/HCO_3^- antiporter and 70% of H^+ generated in the cell is pumped out by the basolateral Na^+/H^+ exchanger (Table 3). These computed results are consistent with recent experimental data obtained from guinea-pig ducts showing: (i) that HCO_3^- secretion in the resting state was dependent on the presence of luminal Cl^-, and (ii) that half of H^+ efflux via the basolateral membrane was amiloride-sensitive [23, 24]. Taken together, these quantitative similarities between computed and experimental data suggest that our updated model accurately mimics the duct cell in the resting steady state.

Stimulated Cell. Patch-clamp studies have shown that the luminal Cl^- conductance of pancreatic duct cells is mediated by CFTR Cl^- channels [11, 15], and Ca^{2+}-activated Cl^- channels [16]. These Cl^- channels are key regulatory points in the HCO_3^- secretory mechanism because they allow recycling of Cl^- through the luminal Cl^-/HCO_3^- exchanger [for reviews *see* 4, 5]. In addition, CFTR channels have a significant permeability to HCO_3^- ions with the measured Cl^-:HCO_3^- permeability ratio being 5:1 [14].

Figure 5*A* shows the effect of altering luminal Cl^- and HCO_3^- permeability ($\omega_{Cl,HCO3(l)}$) and the Na^+-HCO_3^- cotransporter permeability ($G_{Na\text{-}HCO3}$), on the rates of HCO_3^- ($J_{HCO3(l)}$) and Cl^- ($J_{Cl(l)}$) flux across the luminal

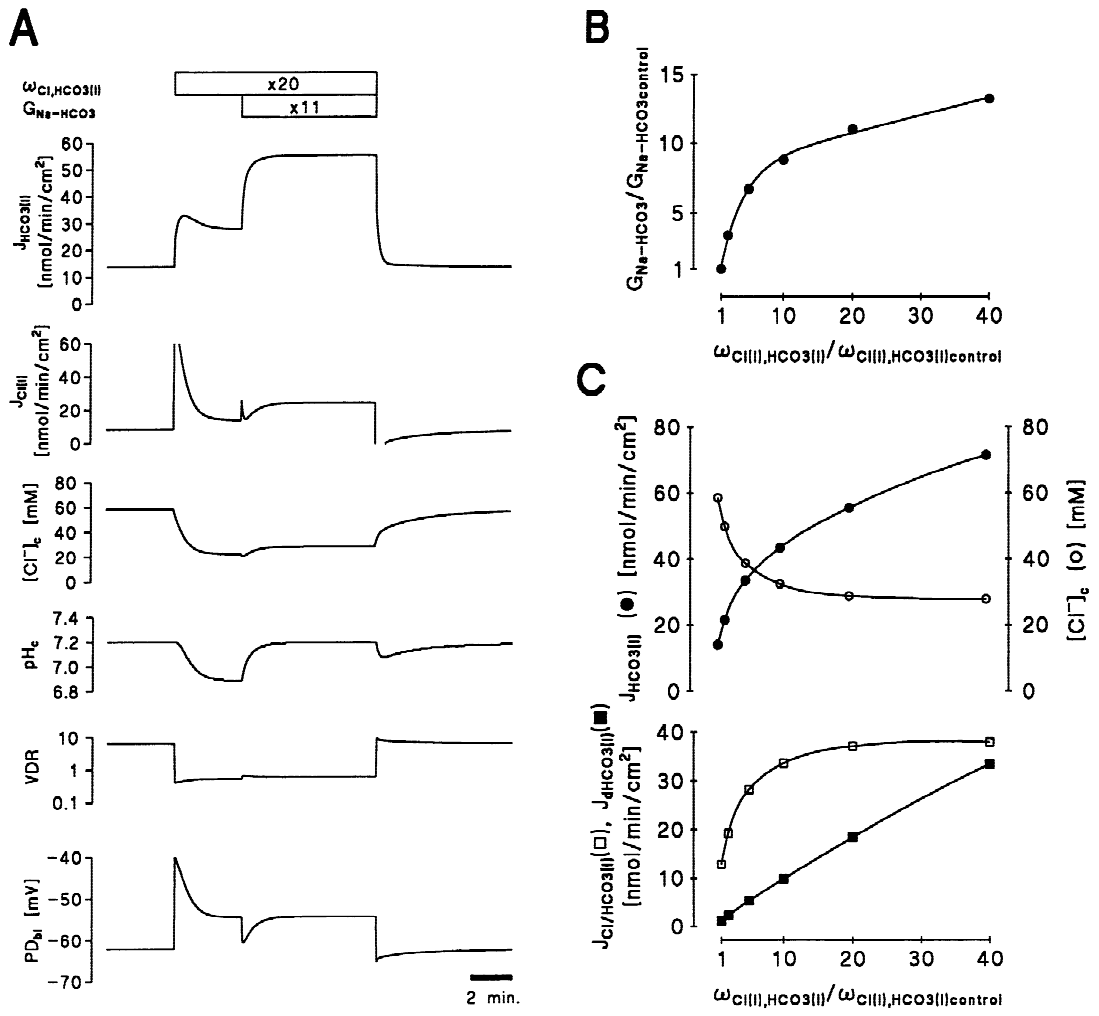

Fig. 5. Computer simulation of a stimulated pancreatic duct cell bathed with symmetrical HCO_3^-/CO_2-buffered solutions, using the nonfluid-secreting 'standard' model. (*A*) Effect of the luminal Cl^- and HCO_3^- conductance ($\omega_{Cl,HCO3(l)}$), and the Na^+-HCO_3^- cotransporter permeability ($G_{Na-HCO3}$), on HCO_3^- flux across the luminal membrane ($J_{HCO3(l)}$), Cl^- flux across the luminal membrane ($J_{Cl(l)}$), intracellular Cl^- concentration ($[Cl^-]_c$), intracellular pH (pH_c), the voltage-divider ratio (*VDR*) and the basolateral potential difference (PD_{bl}). (*B*) Relationship between $\omega_{Cl,HCO3(l)}$ and $G_{Na-HCO3}$ required for keeping pH_c constant at 7.2. (*C*) Summary of the effects of $\omega_{Cl,HCO3(l)}$ on (upper panel) (closed circle) $J_{HCO3(l)}$ and (open circle) $[Cl^-]_c$, and (lower panel) HCO_3^- flux across the luminal membrane via (open square) Cl^-/HCO_3^- antiporter ($J_{Cl/HCO3(l)}$) and (closed square) luminal HCO_3^- conductance ($J_{dHCO3(l)}$), with pH_c being kept constant at 7.2.

membrane, on intracellular Cl^- concentration ($[Cl^-]_c$), intracellular pH (pH_c), the voltage-divider ratio (VDR) and the basolateral potential difference (PD_{bl}). For this stimulation the luminal and basolateral membranes were bathed in the HCO_3^-/CO_2-buffered solution. A 20-fold increase in $\omega_{Cl,HCO3(l)}$ occurs following maximal stimulation of the duct cell with agents that raise intracellular cyclic AMP concentration [15, 29]. Full activation of the luminal anion diffusive pathways ($\omega_{Cl,HCO3(l)}$: ×20) in the model increased $J_{HCO3(l)}$ and $J_{Cl(l)}$, decreased $[Cl^-]_c$, acidified the cell, decreased the VDR and depolarized PD_{bl}. Note that pH_c decreased from 7.20 to 6.89 when $\omega_{Cl,HCO3(l)}$ was increased. However, subsequent activation of the Na^+-HCO_3^- cotransporter ($G_{Na-HCO3}$: ×11) completely reversed this acidification. Activation of the Na^+-HCO_3^- cotransporter also increased $J_{HCO3(l)}$ from 28.0 to 55.5 nmol/min/cm^2 and $J_{Cl(l)}$ from 14.3 to 24.7 nmol/min/cm^2 but surprisingly did not change $[Cl^-]_c$, VDR and PD_{bl}. Model parameters were within the physiological range during this simulation (Table 2).

Previously, it has been reported that stimulation with secretin did not change pH_c in guinea-pig duct cells [23]. Figure 5*B* shows the predicted relationship between $\omega_{Cl,HCO3(l)}$ and $G_{Na-HCO3}$ that would be required for pH_c in the model to remain constant at 7.20 following stimulation.

Figure 5*C* summarizes the effects of various degrees of stimulation (represented by the relative value of

$\omega_{Cl,HCO3(l)}$ above control) on HCO_3^- secretion and on intracellular Cl^- concentration. Stimulation is mimicked by the combined activation of luminal anion diffusive pathways and the basolateral Na^+-HCO_3^- cotransporter. The upper panel in Fig. 5*C* shows the relationship between $\omega_{Cl,HCO3(l)}$ and $J_{HCO3(l)}$, and between $\omega_{Cl,HCO3(l)}$ and $[Cl^-]_c$. Note that as $\omega_{Cl,HCO3(l)}$ increases there is a fall in $[Cl^-]_c$. In contrast, increasing $\omega_{Cl,HCO3(l)}$ leads to an increase $J_{HCO3(l)}$, even in the $\omega_{Cl,HCO3(l)}$ range (>×10) when $[Cl^-]_c$ has fallen to a minimum level. The lower panel in Fig. 5*C* shows the relationship between $\omega_{Cl,HCO3(l)}$ and HCO_3^- flux across the luminal membrane via the Cl^-/HCO_3^- antiporter ($J_{Cl/HCO3(l)}$), and between $\omega_{Cl,HCO3(l)}$ and HCO_3^- flux via the luminal HCO_3^- conductance ($J_{dHCO3(l)}$). Note that as $\omega_{Cl,HCO3(l)}$ increases there is an exponential-like increase in HCO_3^- flux via the antiporter, whereas flux through the conductance pathway increase linearly. These data indicate that HCO_3^- is secreted mainly via the Cl^-/HCO_3^- antiporter in the lower range of $\omega_{Cl,HCO3(l)}$ values (<×10). However, at $\omega_{Cl,HCO3(l)}$ values >×10, the proportion of HCO_3^- secreted by the conductance pathway increases steadily. Because the total HCO_3^- flux across the luminal membrane ($J_{HCO3(l)}$) is the sum of $J_{Cl/HCO3(l)}$ and $J_{dHCO3(l)}$, the biphasic relationship between $\omega_{Cl,HCO3(l)}$ and $J_{HCO3(l)}$ (Fig. 5*C* upper panel) can be explained by the summing of antiporter and conductance fluxes as $\omega_{Cl,HCO3(l)}$ is increased (Fig. 5*C* lower panel). In the maximally stimulated condition ($\omega_{Cl,HCO3(l)}$: ×20 and $G_{Na\text{-}HCO3}$: ×11), the proportion of the total HCO_3^- that is secreted via the luminal HCO_3^- conductance rises from 9% to 33% (Fig. 5*C* lower panel; Table 3). Moreover, 77% of the H^+ generated in the cell is neutralized by HCO_3^- influx via the basolateral Na^+-HCO_3^- cotransporter (Table 3). These simulated data are consistent with recent experimental findings showing that: (i) agonist-evoked HCO_3^- efflux is relatively insensitive to a reduction in luminal Cl^- concentration, and that (ii) 75% of H^+ efflux across the basolateral membrane is blocked by dihydro-4,4′-diisothiocyanostilbene-2,2′-disulfonic acid (H_2DIDS) [23, 24].

Characteristics of Bicarbonate-Rich Fluid Secretion

Next we investigated the characteristics of HCO_3^- secretion by using the fluid-secreting model.

The fluid- secretion model also remained in a steady state at rest with the same parameter set as used in the nonfluid secreting model (Fig. 6). Steady-state values for the variables, fluxes and turnover rates in the fluid-secreting model under each condition are given in Table 4. In the resting steady state, HCO_3^- concentration in the luminal compartment, $[HCO_3^-]_l$, is 38.1 mM and the rate of volume flux into the lumen, J_{vfld}, is 122.3 nl/min/cm^2. Note that the effective HCO_3^- concentration of the secreted fluid, $[HCO_3^-]_{fld}$, is equal to $[HCO_3^-]_l$. This means that the duct cell secretes a fluid containing 38.1 mM HCO_3^- at a rate of 122.3 nl/min/cm^2 in the resting condition.

Initially, maximal stimulation ($\omega_{Cl,HCO3(l)}$: ×20 and $G_{Na\text{-}HCO3}$: ×11) decreases $[Cl^-]_c$ and increases $[HCO_3^-]_{fld}$ and J_{vfld} (Fig. 6*A*). $[HCO_3^-]_l$ also increases following the increases in $[HCO_3^-]_{fld}$ and J_{vfld}. Although $[HCO_3^-]_{fld}$ is higher than $[HCO_3^-]_l$ during the transition from the resting state, $[HCO_3^-]_{fld}$ decreases gradually and becomes equal to $[HCO_3^-]_l$ when the duct cell model reaches a stimulated steady state. Stimulation also decreases $[Cl^-]_c$ from 52.4 to 19.6 mM and increases $[HCO_3^-]_l$ from 38.1 to 67.4 mM and J_{vfld} from 122.3 to 351.9 nl/min/cm^2. Thus the maximum HCO_3^- concentration that can be secreted by the model duct cell under these conditions is about 67 mM. The osmolarity of the luminal fluid (OSM_l) also increases from 319.6 to 327.4 mOsm following stimulation, leading to the increase in J_{vfld} (Table 4). However, fluid secretion by the model can be regarded as isotonic because OSM_l is only 3.8% higher than the basolateral bathing solution (315.5 mOsm). Table 4 also shows that in the stimulated state, model parameters remained within the physiological range. Note that $J_{HCO3(l)}$ in the fluid-secretion model (resting: 4.7; stimulated: 23.7 nmol/min/cm^2, Table 4) is lower than that in the nonfluid-secretion model (resting: 14.0; stimulated: 55.5 nmol/min/cm^2, Table 3). This is because the higher $[HCO_3^-]_l$ (resting: 38.1; stimulated: 67.4 mM) in the fluid-secreting model reduces $J_{Cl/HCO3(l)}$ (resting: 3.4; stimulated: 7.5 nmol/min/cm^2) to a much lower value than in the nonfluid-secreting model (resting: 12.8; stimulated: 37.1 nmol/min/cm^2, $[HCO_3^-]_l$ = 25 mM). However, in the fluid-secreting model the main pathway for HCO_3^- flux across the luminal membrane is still the Cl^-/HCO_3^- antiporter under the resting condition (72% of the total flux) and the HCO_3^- conductance under the stimulated condition (68% of the total flux). Other ion fluxes and transporter turnover rates are not markedly different from those observed in the nonfluid secretion model (Table 3).

After stimulation the duct cell model returns to the resting steady state (Fig. 6*A*). In the transition from the stimulated to the resting state, $[HCO_3^-]_{fld}$ is lower than $[HCO_3^-]_l$, even negative during the initial phase of the transition because HCO_3^- influx via the luminal Cl^-/HCO_3^- antiporters ($J_{Cl/HCO3(l)}$) transiently exceeds HCO_3^- efflux via the luminal HCO_3^- conductance ($J_{dHCO3(l)}$) (Fig. 6*A*).

Figure 6*B* summarizes the effects of stimulation on HCO_3^- secretion, intracellular pH and intracellular Cl^- concentration in the fluid-secreting model. As before, stimulation is mimicked by the combined activation of luminal anion diffusive pathways and the basolateral Na^+-HCO_3^- cotransporter, the degree of stimulation being

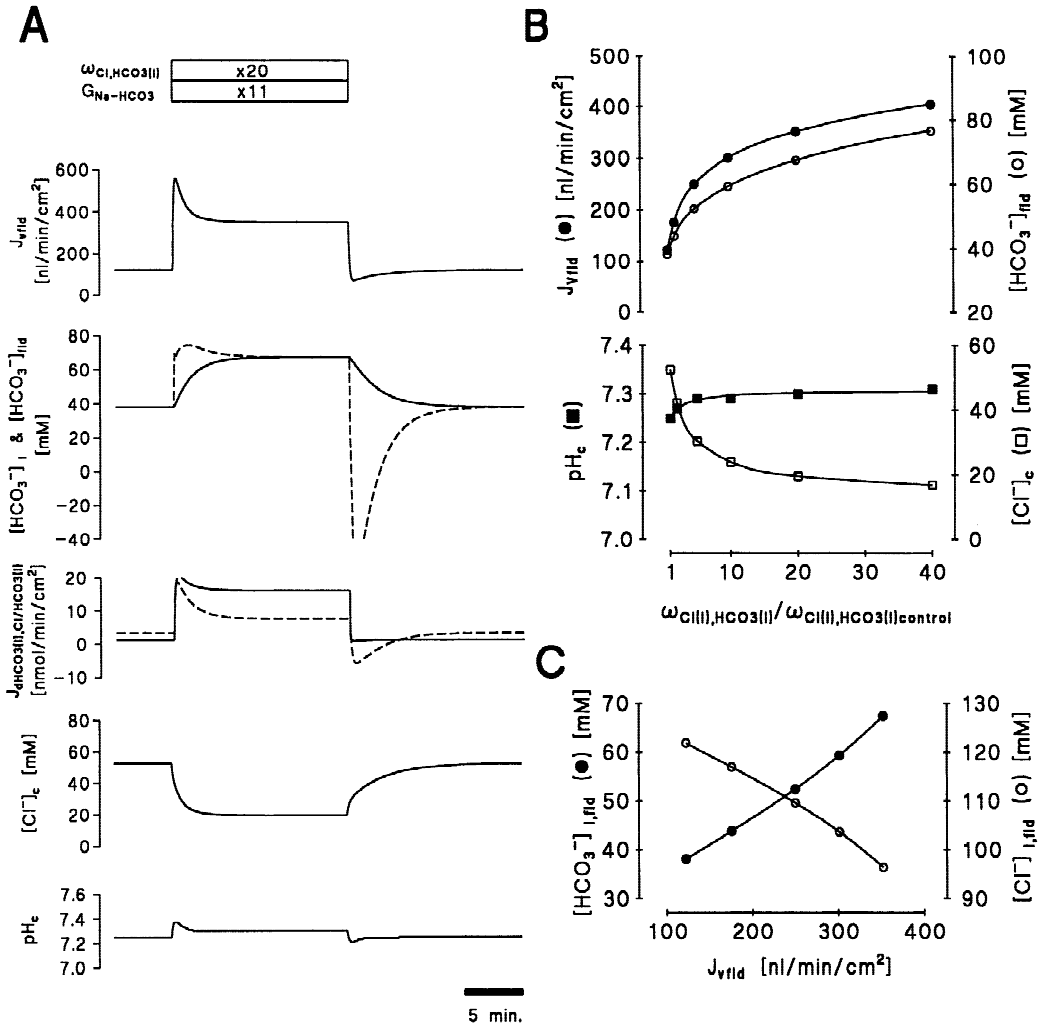

Fig. 6. Computer simulation of HCO_3^--rich fluid secretion in a stimulated pancreatic duct cell, using the fluid-secreting 'standard' model. (*A*) Effect of stimulation on the rate of fluid secretion from the model epithelium (J_{vfld}), (solid line) HCO_3^- concentration of the luminal fluid ($[HCO_3^-]_l$) and (dashed line) HCO_3^- concentration of the secreted fluid ($[HCO_3^-]_{fld}$), (solid line) $J_{dHCO3(l)}$ and (dashed line) $J_{Cl/HCO3(l)}$, $[Cl^-]_c$, and pH_c. The stimulation is mimicked by $\omega_{Cl,HCO3(l)}$: ×20 ($\omega_{Cl(l)} = 6.2 \times 10^{-8}$ cm/sec, $\omega_{HCO3(l)} = 1.24 \times 10^{-8}$ cm/sec) and $G_{Na\text{-}HCO3}$: ×11 ($= 1.65 \times 10^{-8}$ mol/sec/cm^2). (*B*) Summary of the effects of $\omega_{Cl,HCO3(l)}$ on (upper panel) (closed circle) J_{vfld} and (open circle) $[HCO_3^-]_{fld}$, and (lower panel) (closed square) pH_c and (open square) $[Cl^-]_c$ in steady states. The value of $G_{Na\text{-}HCO3}$ shown in Fig. 5*B* at each $\omega_{Cl,HCO3(l)}$ is used for the simulation. Note that $[HCO_3^-]_l$ is equal to $[HCO_3^-]_{fld}$ in steady state. (*C*) Relationship between (closed circle) J_{vfld} and $[HCO_3^-]_{l,fld}$, and between (open circle) J_{vfld} and $[Cl^-]_{l,fld}$. Data over a range of $\omega_{Cl,HCO3(l)}$ from ×1 to ×20 are indicated.

represented by the relative value of $\omega_{Cl,HCO3(l)}$ above control.

Figure 6*B* plots the relationship between the degree of the stimulation and J_{vfld}, $[HCO_3^-]_{l,fld}$, pH_c and $[Cl^-]_c$ in the fluid-secreting model. Stimulation leads to biphasic increases of both J_{vfld} and $[HCO_3^-]_{l,fld}$ (Fig. 6*B* upper panel) corresponding to the biphasic increase of $J_{HCO3(l)}$ (*see* Fig. 5*C* upper panel). As $\omega_{Cl,HCO3(l)}$ increases there is a fall in $[Cl^-]_c$ which reaches a minimum value at about $\omega_{Cl,HCO3(l)}$: ×10, whereas pH_c does not change markedly (Fig. 6*B* lower panel). Over the $[HCO_3^-]_l$ range from 38 to 67 mM, pH_c was changed much less than in the previous version of our pancreatic duct model which did not contain a basolateral Cl^-/HCO_3^- antiporter [36]. This is because HCO_3^- that cannot be secreted against the high luminal HCO_3^- concentration can exit the cell at the basolateral side via the Cl^-/HCO_3^- antiporter (Table 4).

Figure 6*C* shows the relationships between J_{vfld} and $[HCO_3^-]_{l,fld}$ and between J_{vfld} and $[Cl^-]_{l,fld}$. As J_{vfld} increases from 120 (resting) to 350 (stimulated) nl/min/cm^2, $[HCO_3^-]_{l,fld}$ linearly increases from 38 mM to 67 mM and $[Cl^-]_{l,fld}$ linearly decreases from 120 mM to 96 mM. These model data are consistent with experimental findings in that HCO_3^- and Cl^- concentrations in rat pancreatic juice are flow rate dependent and reciprocal, and the maximum HCO_3^- concentration is 60–70 mM [for reviews

Table 4. Values of model variables, volume flux (*nl/min/cm^2 epithelium), ions fluxes and transporter turnover rates (nmol/min/cm^2 epithelium) in resting and stimulated steady states of the fluid-secreting model

Condition	Resting	Stimulated
$[Na^+]_l$ (mM)	154.5	158.3
$[K^+]_l$ (mM)	5.3	5.4
$[Cl^-]_l$ (mM)	121.8	96.4
$[HCO_3^-]_{l,fld}$ (mM)	38.1	67.4
pH_l	7.58	7.83
OSM_l (mOsm)	319.6	327.4
$[Na^+]_c$ (mM)	10.8	11.5
$[K^+]_c$ (mM)	128.7	122.2
$[Cl^-]_c$ (mM)	52.4	19.6
$[HCO_3^-]_c$ (mM)	17.9	20.0
$[X]_c$ (mM)	106.0	143.0
pH_c	7.25	7.30
OSM_c (mOsm)	315.8	316.3
PD_{bl} (mV)	−62.6	−57.1
PD_{te} (mV)	−3.1	−6.7
VDR	7.2	0.8
R_{te} (Ωcm^2)	47.9	41.0
I_{sc} (μA/cm^2)	62.0	157.7
Vol_{cell} (μl/cm^2)	1.22	1.00
J_{vfld}*	122.3	351.9
$J_{HCO3(l)}$	4.7	22.7
$J_{Cl(l)}$	14.9	33.9
$J_{dHCO3(l)}$	1.3	16.2
$J_{dCl(l)}$	18.3	41.4
$J_{Cl/HCO3(l)}$	3.4	7.5
$J_{Cl/HCO3(bl)}$	14.9	33.9
$J_{Na/H}$	13.5	12.1
$J_{Na\text{-}HCO3}$	3.8	43.3
J_{Hpump}	2.2	2.2
$J_{dNa(bl)}$	58.1	54.2
$J_{dK(bl)}$	−49.0	−58.6
$J_{NaKpump}$	24.5	29.3
$J_{Na(j)}$	18.9	55.7
$J_{K(j)}$	0.6	1.9

Turnover rates of H^+/HCO_3^- transporters are converted into their H^+/HCO_3^- transport rates. Bathed with HCO_3^-/CO_2-buffered solution on basolateral side. The stimulation is mimicked by $\omega_{Cl,HCO3(l)}$: ×20 ($\omega_{Cl(l)} = 6.2 \times 10^{-8}$ cm/sec, $\omega_{HCO3(l)} = 1.24 \times 10^{-8}$ cm/sec) and $G_{Na\text{-}HCO3}$: ×11 ($= 1.65 \times 10^{-8}$ mol/sec/cm^2).

see 4, 5]. Taken together, these data show that our duct cell model can reproduce the fluid secretion containing a relatively low HCO_3^- concentration (60–70 mM) found in rat pancreas. We refer to this model as the 'standard' model.

Modelling a Cell That Secretes Fluid with a $[HCO_3^-]$ Greater than 60–70 mM

The maximum HCO_3^- concentration found in pancreatic juice of cats, dogs, guinea pigs and humans is 140–150 mM (*see* Introduction). Therefore, we next investigated what additional assumptions were required to increase the maximum HCO_3^- concentration secreted by the computer model from 60–70 mM to the 140–150 mM secreted by the pancreas of most species.

Step 1: Transport Parameters Required for Secretion of a High HCO_3^- Fluid into a Luminal Solution Containing 25 mM HCO_3^-

As a first step, we sought to identify the conditions that would be required for the model to secrete at high $[HCO_3^-]_{fld}$ (~140 mM) into a luminal solution containing low (25 mM) HCO_3^-, while at the same time maintaining cellular and electrical parameters within the physiological range. In the present model, the concentration of HCO_3^- in the secreted fluid ($[HCO_3^-]_{fld}$) should be affected directly by: (i) the relative activity of the luminal and basolateral Cl^-/HCO_3^- antiporters, and (ii) the HCO_3^-/Cl^- permeability ratio of the luminal membrane. Therefore, we investigated whether changing the activity of these transporters affected $[HCO_3^-]_{fld}$ by using the non-fluid-secreting model bathed in symmetrical solutions containing 25 mM HCO_3^-.

Effects of $G_{Cl/HCO3(l)}$ and $G_{Cl/HCO3(bl)}$. Changing the antiporter distribution ratio (ADR) in favor of the luminal membrane should increase HCO_3^- efflux into, and Cl^- influx from, the lumen via the antiporter and so increase $[HCO_3^-]_{fld}$. Increasing the ADR ($G_{Cl/HCO3(l)}/G_{Cl/HCO3(bl)}$) from 3:2 (1.5) to 9:1 (9) increased $[HCO_3^-]_{fld}$ from ~110 to over 140 mM without changing J_{vfld}, $[Cl^-]_c$ and pH_c (Fig. 7*A*). Figure 7*B* summarizes the effect of $G_{Cl/HCO3(l)}/G_{Cl/HCO3(bl)}$ (ADR) on $[HCO_3^-]_{fld}$ and J_{vfld}. Note that the sum of $G_{Cl/HCO3(l)}$ and $G_{Cl/HCO3(bl)}$ is kept constant at the control value over all conditions tested. Increasing $G_{Cl/HCO3(l)}/G_{Cl/HCO3(bl)}$ (ADR) increases $[HCO_3^-]_{fld}$ exponentially but does not change J_{vfld}. With values of ADR higher than 6, $[HCO_3^-]_{fld}$ exceeds 140 mM, and the model variables stay within the physiological range (Table 5). However it should be noted that with an ADR higher than 10, basolateral Cl^-/HCO_3^- antiporter activity is very low and undetectable by the method of measuring pH_c under Cl^--free conditions shown in Fig. 4*A* (*data not shown*).

Effects of $\omega_{HCO3(l)}$ and $\omega_{Cl(l)}$. Another way of increasing $[HCO_3^-]_{fld}$ in the model is to increase the luminal HCO_3^-/Cl^- permeability ratio ($\omega_{HCO3(l)}/\omega_{Cl(l)}$, LPR). Increasing the LPR from 0.2 to 1 increased $[HCO_3^-]_{fld}$ from ~110 to ~120 mM with model parameters remaining within the physiological range (Fig. 7*A*, Table 5). Figure 7*C* summarizes the effect of LPR on $[HCO_3^-]_{fld}$ and J_{vfld}. Note that $\omega_{HCO3(l)}$ and $\omega_{Cl(l)}$ are changed to keep pH_c constant at 7.2. Under this conditions, increasing LPR increases $[HCO_3^-]_{fld}$ without changing J_{vfld} (Fig. 7*C*). However, compared with ADR, $[HCO_3^-]_{fld}$ is not very sensitive to LPR. This is because the increase in $[Cl^-]_c$

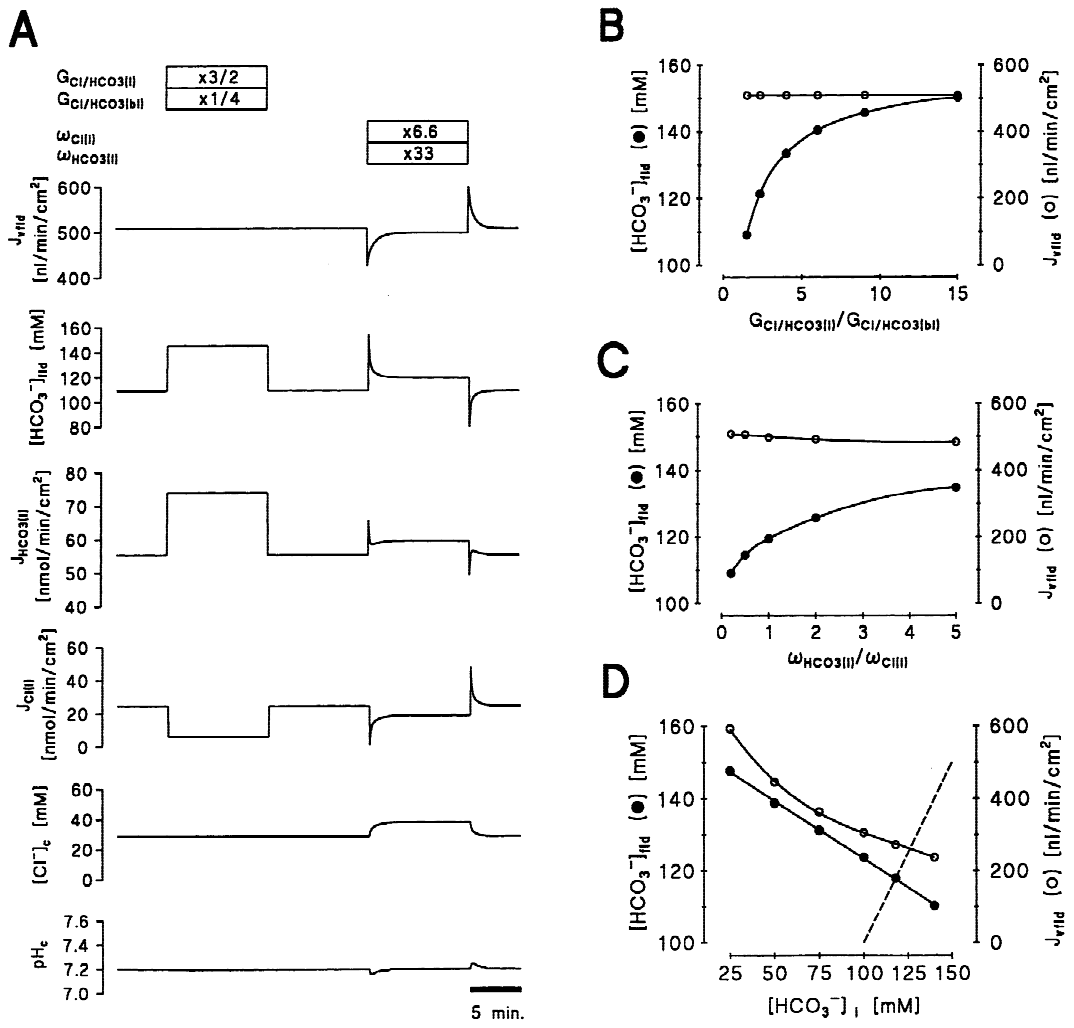

Fig. 7. Modelling the secretion of a high HCO_3^- fluid (>60–70 mM) against fixed luminal HCO_3^- concentrations of 25 mM or greater. Nonfluid-secreting 'high bicarbonate' model of a stimulated pancreatic duct. (*A*) Effect of the ADR and HCO_3^-/Cl^- permeability ratio of luminal membrane (LPR) on J_{vfld}, $[HCO_3^-]_{fld}$, $J_{HCO3(l)}$, $J_{Cl(l)}$, $[Cl^-]_c$, and pH_c under the stimulated condition. The stimulation is basically mimicked by $\omega_{Cl,HCO3(l)}$: ×20 ($\omega_{Cl(l)} = 6.2 \times 10^{-8}$ cm/sec, $\omega_{HCO3(l)} = 1.24 \times 10^{-8}$ cm/sec) and $G_{Na\text{-}HCO3}$: ×11 ($= 1.65 \times 10^{-8}$ mol/sec/cm^2). Note that ADR affects the ratio of Cl^-/HCO_3^- exchange (Cl^- influx and HCO_3^- efflux) activities between the luminal and basolateral membranes, and LPR affects the ratio of Cl^- and HCO_3^- diffusive fluxes across the luminal membrane. ADR ($G_{Cl/HCO3(l)}$: $G_{Cl/HCO3(bl)}$) is changed to 9:1 with $G_{Cl/HCO3(l)}$: ×3/2 and $G_{Cl/HCO3(bl)}$: ×1/4. LPR ($\omega_{Cl(l)}$:$\omega_{HCO3(l)}$) is changed to 1 (1:1) with $\omega_{Cl(l)}$: ×6.6 and $\omega_{HCO3(l)}$: ×33. (*B*) Summary of effects of ADR on (closed circle) $[HCO_3^-]_{fld}$ and (open circle) J_{vfld}. $G_{Cl/HCO3(l)}$ and $G_{Cl/HCO3(bl)}$ are changed with keeping the sum of $G_{Cl/HCO3(l)}$ and $G_{Cl/HCO3(bl)}$ at the control value (1.2×10^{-8} mol/sec/cm^2). Other assumptions: $\omega_{Cl,HCO3(l)}$: ×20 and $G_{Na\text{-}HCO3}$: ×11. (*C*) Summary of effects of LPR on (closed circle) $[HCO_3^-]_{fld}$ and (open circle) J_{vfld}. LPR is changed to 0.2, 0.5, 1, 2 and 5 with $\omega_{Cl(l)}$ and $\omega_{HCO3(l)}$: ×20 and ×20, ×11 and ×27.5, ×6.6 and ×33, ×4 and ×40, and ×2 and ×50, respectively, for keeping pH_c constant at 7.2. Other assumptions: ADR: the control value (3:2) and $G_{Na\text{-}HCO3}$: ×11. (*D*) Summary of the effects of $[HCO_3^-]_l$ on (closed circle) $[HCO_3^-]_{fld}$ and (open circle) J_{vfld} in the stimulated high bicarbonate (nonfluid-secreting) model. See text for assumptions of the high bicarbonate model. The stimulation is mimicked by $\omega_{Cl,HCO3(l)}$: ×20 ($\omega_{Cl(l)} = 6 \times 10^{-8}$ cm/sec, $\omega_{HCO3(l)} = 2.4 \times 10^{-8}$ cm/sec) and $G_{Na\text{-}HCO3}$: ×11 ($= 1.98 \times 10^{-8}$ mol/sec/cm^2). The dashed line in Fig. 7*D* indicates the line of $[HCO_3^-]_l = [HCO_3^-]_{fld}$.

that follows the decrease in $\omega_{Cl(l)}$ reduces $J_{Cl/HCO3(l)}$ (Table 5). Even with LPR ($\omega_{HCO3(l)}$:$\omega_{Cl(l)}$) = 5 (5:1) which is a much higher relative HCO_3^- permeability than previously reported for the CFTR channel [16], $[HCO_3^-]_{fld}$ is still lower than 140 mM. Preliminary patch-clamp experiments [31] have shown that LPR ($\omega_{HCO3(l)}$:$\omega_{Cl(l)}$) in the secretin-stimulated pancreatic duct cells of guinea pig which secretes over 140 mM HCO_3^- is 0.4 (2:5).

Based on the simulation results above, we identified the conditions that would be required for the model to secrete at high $[HCO_3^-]_{fld}$ (~140 mM) into a luminal solution containing low (25 mM) HCO_3^-, as follows: $\omega_{Cl(l)}$: 3×10^{-9} cm/sec and $\omega_{HCO3(l)}$: 1.2×10^{-9} cm/sec (LPR

Table 5. Values of J_{vfld} (*nl/min/cm^2 epithelium), $[HCO_3^-]_{fld}$, ions fluxes and transporter turnover rates (nmol/min/cm^2 epithelium), and model variables in stimulated steady states of the nonfluid-secreting model with additional assumptions

$\omega_{HCO3(l)}$	×20	×20	×33
$\omega_{Cl(l)}$	×20	×20	×6.6
$G_{Cl/HCO3(l)}$	×1	×3/2	×1
$G_{Cl/HCO3(bl)}$	×1	×1/4	×1
J_{vfld}*	508.7	508.7	499.1
$[HCO_3^-]_{fld}$ (mM)	109.1	145.6	119.5
$J_{HCO3(l)}$		74.1	59.7
$J_{Cl(l)}$		6.2	19.1
$J_{dHCO3(l)}$		18.4	31.0
$J_{dCl(l)}$		61.9	47.7
$J_{Cl/HCO3(l)}$		55.7	28.6
$J_{Cl/HCO3(bl)}$		6.2	19.1
$[Na^+]_c$ (mM)		12.0	12.0
$[K^+]_c$ (mM)		120.5	122.6
$[Cl^-]_c$ (mM)		28.8	38.4
$[HCO_3^-]_c$ (mM)		15.7	15.8
$[X]_c$ (mM)		138.5	126.7
pH_c		7.20	7.20
PD_{bl} (mV)		−54.2	−54.8
PD_{te} (mV)		−6.6	−6.4
VDR		0.6	1.3
I_{sc} (μA/cm^2)		157.9	147.0
Vol_{cell} (μl/cm^2)		1.02	1.08

Turnover rates of H^+/HCO_3^- transporters are converted into their H^+/HCO_3^- transport rates. Bathed with HCO_3^-/CO_2-buffered solution on both luminal and basolateral side. Other assumptions for stimulation: $G_{Na\text{-}HCO3}$: ×11 (= 1.65×10^{-8} mol/sec/cm^2).

(ω_{HCO3}:ω_{Cl}) = 2:5), $G_{Cl/HCO3(l)}$: 1.08×10^{-8} mol/sec/cm^2 and $G_{Cl/HCO3(bl)}$: 1.2×10^{-9} mol/sec/cm^2 (ADR = 9:1), and $G_{Na\text{-}HCO3}$: 1.8×10^{-8} mol/sec/cm^2 (for pH_c = 7.2). All other parameters are identical to the standard model. We next checked the basic characteristics of ion transport and fluid secretion using this new parameter set. We refer to this model as the 'high bicarbonate' model.

Basic Characteristics of Ion Transport in the 'High Bicarbonate' Model. Table 6 shows steady-state values for the fluxes, turnover rates and variables in the high bicarbonate (nonfluid-secreting) model under each condition. With symmetrical 25 mM HCO_3^- solutions, the model remained in a steady state at rest and maximal stimulation ($\omega_{Cl,HCO3(l)}$: ×20 and $G_{Na\text{-}HCO3}$: ×11) decreases $[Cl^-]_c$ from 59.1 to 30.7 mM and increases J_{vfld} about 4-fold from 147.4 to 593.2 nl/min/cm^2. At the same time, $[HCO_3^-]_{fld}$ increases slightly from 143.6 to 147.7 mM (Table 6). In both resting and stimulated conditions, the cellular and electrical variables of the high bicarbonate (nonfluid-secreting) model are maintained within the physiological range (Table 6).

Taken together, these data show that provided the luminal $[HCO_3^-]$ is held constant at 25 mM the 'high bicarbonate' model will secrete a fluid containing ~140 mM HCO_3^-, i.e., close to the maximum concentration of HCO_3^- found in pancreatic juice under physiological conditions.

Step 2: What Happens When the Luminal $[HCO_3^-]$ is Allowed to Rise Above 25 mM?

Next, we investigated the effects of increasing luminal $[HCO_3^-]$ on the basic characteristics of ion transport in the 'high bicarbonate' model. Figure 7*D* summarizes the effects of $[HCO_3^-]_l$ on $[HCO_3^-]_{fld}$ and J_{vfld} in the stimulated condition. Increasing $[HCO_3^-]_l$ from 25 mM to 140 mM (luminal Cl^- being replaced with HCO_3^-) decreases $[HCO_3^-]_{fld}$ from 147.7 to 110.3 mM. At the same time, J_{vfld} decreases from 593.2 to 237.8 nl/min/cm^2 (Fig. 7*D*), mainly because of a decrease in $J_{Cl/HCO3(l)}$ (*see* Table 6). With a $[HCO_3^-]_l$ of less than 118.0 mM, $[HCO_3^-]_{fld}$ is higher than $[HCO_3^-]_l$. However, if $[HCO_3^-]_l$ is greater than 118.0 mM, $[HCO_3^-]_{fld}$ is lower than $[HCO_3^-]_l$ (Fig. 7*D*). This means that the maximum HCO_3^- concentration that can be secreted by the 'high bicarbonate' (nonfluid-secreting) model is around 118 mM. Although increasing $[HCO_3^-]_l$ also increases pH_c, the model variables including pH_c are still maintained within the physiological range over all conditions tested (Table 6).

Bicarbonate-rich Fluid Secretion in the 'High Bicarbonate' Model. Next we investigated the characteristics of HCO_3^--rich fluid secretion by the 'high bicarbonate' model. The 'high bicarbonate' fluid-secreting model remained in a steady state at rest (Fig. 8*A*). Steady-state values for the variables, fluxes and turnover rates in the high bicarbonate (fluid-secreting) model under each condition are shown in Table 7. In the resting steady state, the high bicarbonate (fluid-secreting) model secretes a fluid containing 67.1 mM HCO_3^- to the lumen in which $[HCO_3^-]$ is 67.1 mM at a rate of 83.4 nl/min/cm^2. Maximal stimulation ($\omega_{Cl,HCO3(l)}$: ×20 and $G_{Na\text{-}HCO3}$: ×11) increases $[HCO_3^-]_{t,fld}$ from 67.1 to 119.7 mM to 119.7 mM and J_{vfld} about 3-fold from 83.4 to 251.4 nl/min/cm^2. The simulated rate of fluid secretion is comparable with experimental data obtained from isolated guinea-pig pancreatic ducts (resting: ~1 nl/min/mm^2, stimulated: ~3 nl/min/mm^2) [22]. Note that cellular and electrical variables in the resting and stimulated conditions are within the physiological range, although pHc (resting: 7.39; stimulated: 7.39) is higher than that when the cell is bathed with symmetrical solutions containing 25 mM HCO_3^- (7.2). Under stimulated conditions, HCO_3^- efflux via the luminal HCO_3^- conductance was 94% of total luminal HCO_3^- efflux and 71% of the H^+ generated in the cell was neutralized by HCO_3^- influx via Na^+-HCO_3^- cotransporters (Table 7). These simulated data are consistent with recent experimental findings [23, 24].

Taken together, our data show when the luminal $[HCO_3^-]$ is allowed to rise, the maximum HCO_3^- concen-

Table 6. Values of J_{vfld} (*nl/min/cm^2 epithelium), $[HCO_3^-]_{fld}$, ions fluxes and transporter turnover rates (nmol/min/cm^2 epithelium), and model variables in resting and stimulated steady states of the high bicarbonate (nonfluid-secreting) model

Condition	Resting	Stimulated		
$[HCO_3^-]_l$ (mM)	25	25	118	140
J_{vfld}*	147.4	593.2	272.7	237.8
$[HCO_3^-]_{fld}$ (mM)	143.6	147.7	118.0	110.3
$J_{HCO3(l)}$	21.2	87.6	32.2	26.2
$J_{Cl(l)}$	2.1	5.9	10.8	11.3
$J_{dHCO3(l)}$	2.4	34.1	30.9	27.0
$J_{dCl(l)}$	20.9	59.5	12.1	10.5
$J_{Cl/HCO3(l)}$	18.8	53.5	1.3	−0.8
$J_{Cl/HCO3(bl)}$	2.1	5.9	10.8	11.3
$J_{Na/H}$	15.1	14.5	10.3	10.0
$J_{Na\text{-}HCO3}$	5.3	75.5	31.3	26.2
J_{Hpump}	2.8	3.6	1.5	1.4
$J_{dNa(bl)}$	57.7	51.3	55.2	55.6
$J_{dK(bl)}$	−50.3	−69.0	−54.1	−52.4
$J_{NaKpump}$	25.2	34.5	27.0	26.2
$J_{Na(j)}$	22.5	90.5	41.6	36.3
$J_{K(j)}$	0.8	3.1	1.4	1.2
$[Na^+]_c$ (mM)	10.9	12.3	11.1	11.0
$[K^+]_c$ (mM)	129.0	121.5	121.1	120.9
$[Cl^-]_c$ (mM)	59.1	30.7	5.5	2.4
$[HCO_3^-]_c$ (mM)	15.7	16.0	24.1	25.0
$[X]_c$ (mM)	100.8	135.0	153.7	156.2
pH_c	7.20	7.20	7.38	7.40
PD_{bl} (mV)	−62.1	−53.1	−58.5	−59.1
PD_{te} (mV)	−1.9	−7.7	−3.5	−3.1
VDR	6.6	0.6	1.3	1.5
I_{sc} (μA/cm^2)	38.8	187.1	80.5	69.3
Vol_{cell} (μl/cm^2)	1.26	1.04	0.96	0.95

Turnover rates of H^+/HCO_3^- transporters are converted into their H^+/HCO_3^- transport rates. Bathed with 25 mM HCO_3^-/CO_2-buffered solution on basolateral side. The stimulation is mimicked by $\omega_{Cl,HCO3(l)}$: ×20 ($\omega_{Cl(l)} = 6 \times 10^{-8}$ cm/sec, $\omega_{HCO3(l)} = 2.4 \times 10^{-8}$ cm/sec) and $G_{Na\text{-}HCO3}$: ×11 ($= 1.98 \times 10^{-8}$ mol/sec/cm^2).

tration in the fluid secreted by this version of the model is about 118 mM, i.e., somewhat less than the maximum concentration of HCO_3^- found in the pancreatic juice of most species (~140 mM).

Step 3: Additional Assumptions Required for Secretion of a Fluid Containing 140 mM HCO_3^- into a Luminal Solution Containing 140 mM HCO_3^-

To secrete a pancreatic juice containing 140 mM HCO_3^- constantly, the duct cell must be able to secrete a fluid of $[HCO_3^-]_{fld} = 140$ mM against a luminal solution containing 140 mM HCO_3^-. Therefore, we sought to identify the additional assumptions required to allow the model to work in this way. We reasoned that in the stimulated steady state of the 'high bicarbonate' model, $[HCO_3^-]_{fld}$ should be affected directly by: (i) the activity of the luminal Cl^-/HCO_3^- antiporter, and (ii) the HCO_3^- and Cl^- permeability of the luminal membrane.

Effects of $\omega_{Cl(l)}$ and $G_{Cl/HCO3(l)}$. Preliminary patch-clamp experiments have shown that an increase in luminal $[HCO_3^-]$ reduces the luminal Cl^- conductance in guinea-pig duct cells [31]. We incorporated this experimental finding into the model and tested the effect of decreasing $\omega_{Cl(l)}$ on $[HCO_3^-]_{fld}$ and J_{vfld}.

Figure 8*A* shows the effects of manipulating $\omega_{Cl(l)}$ and $G_{Cl/HCO3(l)}$ on J_{vfld}, $[HCO_3^-]_{l,fld}$, $[Cl^-]_c$, pH_c and PD_{bl} in the stimulated high bicarbonate (fluid-secreting) model. Decreasing $\omega_{Cl(l)}$ from ×20 to ×0.05 decreased $J_{dCl(l)}$ from 12.4 to 0.3 nmol/min/cm^2 (Table 7). However decreasing $\omega_{Cl(l)}$ also increased $[Cl^-]_c$ which in turn increased HCO_3^- influx and Cl^- efflux via the luminal Cl^-/HCO_3^- antiporter from 1.8 to 9.1 nmol/min/cm^2. As a result, decreasing $\omega_{Cl(l)}$ from ×20 to ×0.05 caused a small decrease in $[HCO_3^-]_{fld}$ from 119.7 to 118.2 mM (Table 7). At the same time J_{vfld} fell from 251.4 to 217.3 nl/min/cm^2. Thus increasing the relative HCO_3^- permeability of the luminal membrane alone would not enable the model cell to secrete a fluid containing 140 mM into a lumen containing the same concentration of the anion. The principle reason for this is that when the Cl^- permeability of the luminal membrane is decreased, the absorptive HCO_3^- flux on the luminal antiporter limits the HCO_3^- secretory capacity of the cell.

Next we tested the effect of decreasing $G_{Cl/HCO3(l)}$ from ×1 to ×0.0425 which reduced HCO_3^- influx and Cl^- efflux via the antiporter from −9.1 to −2.7 nmol/min/cm^2 (Table 7). This caused a small decrease in J_{vfld} from 217.3 to 196.0 nl/min/cm^2 and at the same time $[HCO_3^-]_{fld}$ increased substantially from 118.2 to 140.0 mM (Fig. 8*A*, Table 7). The rate of fluid secretion in the model is consistent with experimental data (~2 nl/min/mm^2) obtained from guinea-pig ducts in the presence of a high $[HCO_3^-]_l$ [22]. Thus the cell is now secreting fluid (albeit at a low rate) that contains 140 mM HCO_3^- into a luminal solution containing the same concentration of the anion. Note that cellular parameters remained within the physiological range under these conditions, and, as expected, the HCO_3^- ions are secreted via the HCO_3^- conductance (Table 7). Therefore, in order to secrete a 140 mM HCO_3^- fluid into a 140 mM HCO_3^- luminal solution, the basic 'high bicarbonate' fluid secretion-model (120 mM HCO_3^- secretion into a 120 mM HCO_3^- luminal solution: *see* above) must be modified to incorporate inhibition of the luminal Cl^- diffusive pathway and the luminal Cl^-/HCO_3^- antiporter activity (decreasing $\omega_{Cl(l)}$ and $G_{Cl/HCO3(l)}$). Figure 8*B* shows the relationship between $\omega_{Cl(l)}$, and $G_{Cl/HCO3(l)}$ required for keeping $[HCO_3^-]_{l,fld}$ at 140 mM in the stimulated 'high bicarbonate' (fluid secreting) model. Note that with any combination of $\omega_{Cl(l)}$ and $G_{Cl/HCO3(l)}$ shown in Fig. 8*B*, J_{vfld}, pH_c and $[Cl^-]_c$ are not remarkably changed over the range of $\omega_{Cl(l)}$ ($G_{Cl/HCO3(l)}$) from ×0 (×0.0625) to ×0.16 (×0) (Fig. 8*C*).

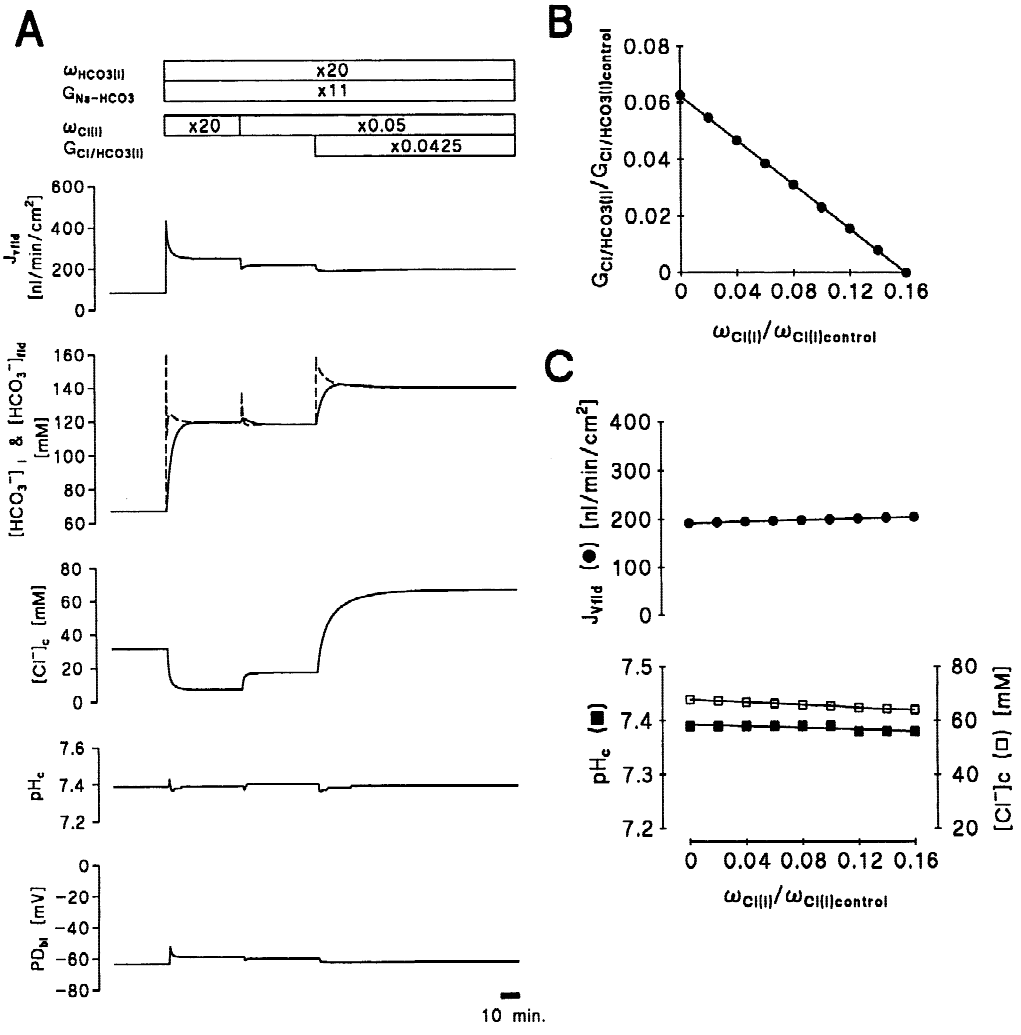

Fig. 8. Modelling the secretion of a high HCO_3^- fluid (140 mM) against a luminal HCO_3^- concentration of 140 mM. Fluid-secreting 'high bicarbonate' model of a stimulated pancreatic duct. (*A*) Effect of $\omega_{Cl(l)}$ and $G_{Cl/HCO3(l)}$ on J_{vfld}, (solid line) $[HCO_3^-]_l$, and (dashed line) $[HCO_3^-]_{fld}$, $[Cl^-]_c$, pH_c and PD_{bl} in the stimulated high bicarbonate (fluid secreting) model. The stimulation is basically mimicked by $\omega_{Cl,HCO3(l)}$: ×20 ($\omega_{Cl(l)} = 6 \times 10^{-8}$ cm/sec, $\omega_{HCO3(l)} = 2.4 \times 10^{-8}$ cm/sec) and $G_{Na\text{-}HCO3}$: ×11 ($= 1.98 \times 10^{-8}$ mol/sec/cm^2). Note that $[HCO_3^-]_l$ is equal to $[HCO_3^-]_{fld}$ in steady states. (*B*) Relationship between $\omega_{Cl(l)}$ and $G_{Cl/HCO3(l)}$ required for keeping $[HCO_3^-]_{l,fld}$ at 140 mM in the stimulated high bicarbonate (fluid-secreting) model. (*C*) Summary of the effects of $\omega_{Cl(l)}$ on (upper panel) (closed circle) J_{vfld}, (lower panel) (closed square) pH_c and (open square) $[Cl^-]_c$ under the condition of $[HCO_3^-]_{l,fld} = 140$ mM in the stimulated high bicarbonate (fluid-secreting) model. $[HCO_3^-]_{l,fld}$ is kept at 140 mM by changing $G_{Cl/HCO3(l)}$ as shown in Fig. 8*B*.

To summarize this section, our modelling data suggest that a pancreatic duct cell equipped with the transport elements shown in Fig. 1 could secrete a fluid containing 140 mM $[HCO_3^-]$ into luminal solutions containing low (25 mM) and high (140 mM) HCO_3^- concentrations. The two changes that need to occur in order to allow the duct cell to secrete into a high HCO_3^- solution (as must occur physiologically) are a decrease in the luminal Cl^- permeability and an inhibition of the luminal anion exchanger. Note that J_{vfld} is markedly reduced when the duct cell is facing a high (140 mM) luminal HCO_3^- concentration, nevertheless net secretion does occur under these conditions (Table 7). We conclude that the cellular model shown in Fig. 1 could, without any additional transport elements, secrete a pancreatic juice containing near isotonic $NaHCO_3$. To achieve this there must be coordinated regulation of the transport elements so as to maintain net secretion of a HCO_3^--rich fluid as the luminal HCO_3^- concentration increases.

A New Hypothesis for the Secretion of a Fluid Containing 140 mM HCO_3^- by the Pancreatic Ductal Epithelium

The hypothesis is summarized in Fig. 9. We view the starting point for the HCO_3^- secretory process as the se-

Table 7. Values of model variables, J_{vfld} (*nl/min/cm^2 epithelium), ions fluxes and transporter turnover rates (nmol/min/cm^2 epithelium) in the high bicarbonate (fluid-secreting) model under the resting, and three different stimulated conditions

	Resting	Stimulated		
$\omega_{Cl(l)}$	×1	×20	×0.05	×0.05
$G_{Cl/HCO3(l)}$	×1	×1	×1	×0.0425
$[Na^+]_l$ (mM)	153.9	156.6	156.1	155.7
$[K^+]_l$ (mM)	5.3	5.4	5.3	5.3
$[Cl^-]_l$ (mM)	92.1	42.3	43.2	21.0
$[HCO_3^-]_{l,fld}$ (mM)	67.1	119.7	118.2	140.0
pH_l	7.83	8.08	8.07	8.15
OSM_l (mOsm)	318.3	324.0	322.9	322.1
$[Na^+]_c$ (mM)	10.5	11.1	11.0	11.1
$[K^+]_c$ (mM)	127.1	121.8	124.0	133.5
$[Cl^-]_c$ (mM)	31.4	7.1	17.1	66.5
$[HCO_3^-]_c$ (mM)	24.6	24.4	24.9	24.3
$[X]_c$ (mM)	122.1	151.7	139.0	80.5
pH_c	7.39	7.39	7.40	7.39
OSM_c (mOsm)	315.7	316.1	316.0	315.9
PD_{bl} (mV)	−63.2	−59.0	−60.1	−62.5
PD_{te} (mV)	−2.5	−5.1	−4.6	−4.2
VDR	9.3	1.1	2.0	1.9
I_{sc} (μA/cm^2)	49.4	117.7	100.8	93.8
Vol_{cell} (μl/cm^2)	1.11	0.97	1.02	1.47
J_{vfld}*	83.4	251.4	217.3	196.0
$J_{HCO3(l)}$	5.6	30.1	25.7	27.4
$J_{Cl(l)}$	7.7	10.6	9.4	4.1
$J_{dHCO3(l)}$	3.2	28.3	34.8	30.1
$J_{dCl(l)}$	10.0	12.4	0.3	1.4
$J_{Cl/HCO3(l)}$	2.4	1.8	−9.1	−2.7
$J_{Cl/HCO3(bl)}$	7.7	10.6	9.4	4.1
$J_{Na/H}$	10.2	10.2	10.0	10.2
$J_{Na\text{-}HCO3}$	1.8	29.1	23.8	20.1
J_{Hpump}	1.2	1.4	1.3	1.3
$J_{dNa(bl)}$	58.5	55.5	56.3	58.0
$J_{dK(bl)}$	−46.4	−53.5	−52.1	−52.2
$J_{NaKpump}$	23.2	26.7	26.1	26.1
$J_{Na(j)}$	12.8	39.4	33.9	30.5
$J_{K(j)}$	0.4	1.3	1.2	1.0

Turnover rates of H^+/HCO_3^- transporters are converted into their H^+/HCO_3^- transport rates. Bathed with HCO_3^-/CO_2-buffered solution on basolateral side. Other assumptions for stimulation, $\omega_{HCO3(l)}$: ×20 (= 2.4×10^{-8} cm/sec) and $G_{Na\text{-}HCO3}$: ×11 (= 1.98×10^{-8} mol/sec/cm^2).

cretion (by the acini) of a small volume of a plasmalike fluid (containing 25 mM HCO_3^-) into the top of the ductal system.

Programming the currently available experimental data into the computer model shows that the cell depicted in Fig. 1 will, provided the antiporter distribution ratio is about 9:1 in favor of the luminal membrane and the HCO_3^-/Cl^- permeability ratio of luminal membrane ($\omega_{HCO3(l)}$:$\omega_{Cl(l)}$) is 2:5, produce a relatively large volume of secretion with a high HCO_3^- concentration (Fig. 8) and increase the HCO_3^- content of the lumen to about 120 mM (Fig. 8). We call this cell the proximal cell, predict that it exists in the upper part of the ductal system close to the acini, and note that it represents one end of a functional spectrum within the ductal tree (Fig. 9).

As the fluid flows along the first part of the ductal system, the luminal HCO_3^- concentration will rise and the net secretory flux of HCO_3^- from the proximal cell will fall (Fig. 7*D*). We propose that as this occurs, the activity of membrane transporters in the proximal cell is progressively modified to those of a cell that can maintain a small net secretory flux of HCO_3^- in the face of near isotonic $NaHCO_3$ in the lumen (Fig. 8). We call this cell the distal cell and note that it represents the other end of the functional spectrum that exists in the ducts. Essentially, the high HCO_3^- secretion produced by the distal cells would dilute out the chloride in the secretions produced by proximal cells in the upper regions of the ductal tree. Compared to proximal cells, the major changes in the transport parameters that allow the distal cells to secrete in the face of a high luminal HCO_3^- concentration are: (i) a reduced luminal Cl^- permeability, and (ii) a reduced activity of the luminal Cl^-/HCO_3^- antiporter (Fig. 8). Thus HCO_3^- secretion would occur mainly by the exchanger in duct segments near the acini (proximal cells), but mainly via the channels further down the ductal tree (distal cells).

Future Experimental Studies

We predict that the functional switch from proximal to distal cell is controlled by signals (e.g., $[HCO_3^-]$ or pH) derived from the duct lumen. We have previously shown that an increase in extracellular $[HCO_3^-]$ reduces the Cl^- conductance of guinea-pig duct cells [31], however, there are no experimental data available concerning inhibition of the luminal Cl^-/HCO_3^- antiporter. Experimental studies designed to test our prediction that the luminal Cl^-/HCO_3^- antiporter is inhibited by high $[HCO_3^-]$ or pH are therefore required.

The mechanism by which extracellular HCO_3^- inhibits the Cl^- conductance in pancreatic duct cells is unknown. Both the Cl^- and HCO_3^- conductances on the luminal membrane probably reside within the same anion channels (i.e., CFTR- and Ca^{2+}-activated Cl^- channels). This means that signals from the duct lumen would have to change the characteristics of ion permeation through these channels. This might come about from multi-ion characteristics. In this respect it is interesting to note that CFTR is known to be a multi-ion channel CFTR [26]. However, we should be clear that decreasing $\omega_{Cl(l)}$ does not imply a change in the anion selectivity of the duct cell luminal membrane. The necessity of decreasing $\omega_{Cl(l)}$ comes only from the requirement for a lower Cl^- as compared to HCO_3^- efflux across the luminal membrane at negative membrane potentials (~ −50 mV), and not from a requirement to increase the

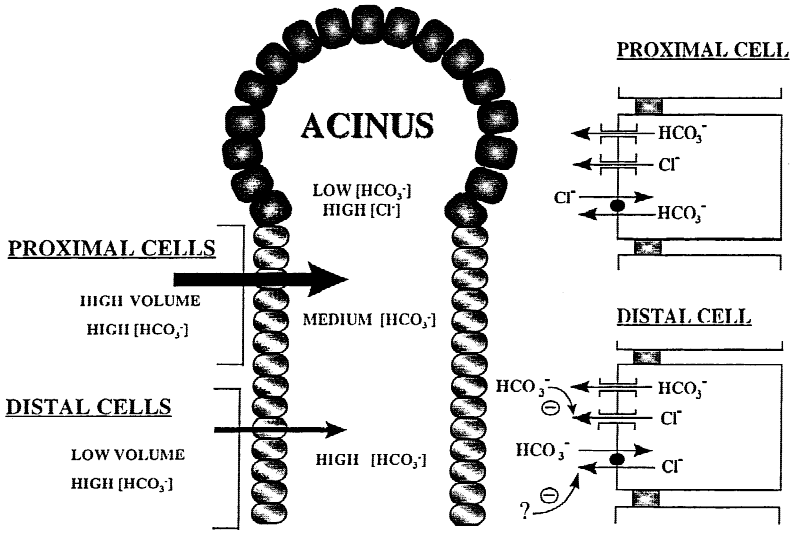

Fig. 9. Schematic representation of the new hypothesis for the secretion of a HCO_3^--rich fluid by the pancreatic ductal tree. *See* text for details.

anion selectivity of the apical membrane to HCO_3^- over Cl^-. Indeed, our preliminary patch-clamp study [31] showed that high extracellular [HCO_3^-] did not change the Cl^-: HCO_3^- selectivity ratio of CFTR channels in guinea-pig pancreatic duct cells, although Cl^- efflux at negative membrane potentials was inhibited markedly. It is, therefore, important to measure the ratio of Cl^- to HCO_3^- effluxes across the luminal membrane of the duct cell under defined experimental conditions and to compare those data with values predicted by the model. Also, we should note that a large conductance anion channel with a Cl^-:HCO_3^- permeability ratio of 1:1 has been identified on CAPAN-1 cell (a human pancreatic cancer cell line of duct origin), although its contribution to luminal anion conductance and its regulation are still unknown [27]. This channel and/or other as yet unidentified anion channels might make a significant contribution to the luminal anion permeability of the duct cell in some conditions.

Conclusion

We have developed an upgraded version of our original computer model of the pancreatic ductal epithelium [36], which includes all the transport elements shown in Fig. 1. Programming the currently available experimental data showed that the model duct cell could secrete a relatively large volume of a HCO_3^--rich fluid, but could only raise the luminal HCO_3^- concentration up to about ~70 mM. Increasing the HCO_3^-/Cl^- permeability ratio of the luminal membrane, and the luminal Cl^-/HCO_3^- exchange activity relative to the basolateral membrane, increased the maximum HCO_3^- concentration in the secreted fluid up to ~118 mM. However, this is still less than the 140 mM HCO_3^- found in the pancreatic juice of most species. Two additional changes in the transport parameters are required for the model duct cell to raise the luminal HCO_3^- concentration up to 140 mM: (i) a reduced luminal Cl^- permeability, and (ii) a reduced activity of the luminal Cl^-/HCO_3^- antiporter.

Our computer modelling studies have allowed us to develop a new hypothesis for the production of a HCO_3^--rich pancreatic juice. We propose: (i) that the pancreatic ductal system can produce an isotonic HCO_3^--rich fluid without any additional transport elements to those shown in Fig. 1, (ii) that HCO_3^- secretion occurs mainly by the antiporter in duct segments near the acini (luminal HCO_3^- concentration up to ~70 mM), but mainly via channels further down the ductal tree (raising luminal HCO_3^- to ~140 mM), and (iii) that changes in the composition of the luminal fluid as it flows along the ductal system modulate the transport characteristics of the duct cells (as described above) so that secretion of a HCO_3^--rich fluid is maintained. An important goal now is to test experimentally the predictions made by the mathematical model, particularly whether signals from the duct lumen inhibit the luminal Cl^-/HCO_3^- antiporter and change the characteristics of ion permeation through the luminal membrane anion channels.

This research was funded by the Cystic Fibrosis Trust and the Medical Research Council (UK).

References

1. Akiba, T., Alpern, R.J., Eveloff, J., Calamina, J., Warnock, D.J. 1986. Electrogenic sodium/bicarbonate cotransporter in rabbit renal cortical basolateral membrane vesicles. *J. Clin. Invest.* **78:**1472–1478
2. Apell, H.J. 1989. Electrogenic properties of the Na,K pump. *J. Membrane Biol.* **110:**103–114
3. Argent, B.E., Arkle, S., Cullen, M.J., Green, R. 1986. Morpho-

logical, biochemical and secretory studies on rat pancreatic ducts maintained in tissue culture. *Q. J. Exp. Physiol.* **71:**633–648
4. Argent, B.E., Case, R.M. 1994. Pancreatic ducts. Cellular mechanism and control of bicarbonate secretion. *In:* Physiology of the Gastrointestinal Tract. 3rd ed. L.R. Johnson, editor. pp. 1473–1497. Raven Press, New York
5. Argent, B.E., Gray, M.A. 1997. Regulation and formation of fluid and electrolyte secretions by pancreatic ductal epithelium. *In:* Biliary and Pancreatic Ductal Epithelia: Pathobiology and Pathophysiology. A.E. Sirica and D.S. Longnecker, editors. pp. 349–377. Marcel Dekker, New York
6. Boron, W.F., Hediger, M.A., Boulpaep, E.L., Romero, M.F. 1997. The renal electrogenic Na^+:HCO_3^- cotransporter. *J. Exp. Biol.* **200:**263–268
7. Cole, K.S. 1968. Linear and passive cell properties. *In:* Membranes, Ions and Impulses. pp. 5–114. University of California Press, Berkeley
8. Davies, J.M., Sanders, D., Gradmann, D. 1996. Reaction kinetics of the vacuolar H^+-pumping ATPase in *Beta vulgaris. J. Membrane Biol.* **150:**231–241
9. de Ondaraza, J., Hootman, S.R. 1997. Confocal microscopic analysis of intracellular pH regulation in isolated guinea pig pancreatic ducts. *Am. J. Physiol.* **272:**G124–G134
10. Ehrenfeld, J., Garcia-Romeu, F., Harvey, B.J. 1985. Electrogenic active proton pump in rana esculenta skin and its role in sodium ion transport. *J. Physiol.* **359:**331–355
11. Gray, M.A., Greenwell, J.R., Argent, B.E. 1988. Secretin-regulated chloride channel on the apical membrane of pancreatic duct cells. *J. Membrane Biol* **105:**131–142
12. Gray, M.A., Argent, B.E. 1990. Non-selective cation channel on pancreatic duct cells. *Biochim. Biophys. Acta* **1029:**33–42
13. Gray, M.A., Greenwell, J.R., Garton, A.J., Argent, B.E. 1990. Regulation of maxi-K^+ channels on pancreatic duct cells by cyclic AMP-dependent phosphorylation. *J. Membrane Biol.* **115:**203–215
14. Gray, M.A., Pollard, C.E., Harris, A., Coleman, L., Greenwell, J.R., Argent, B.E. 1990. Anion selectivity and block of the small-conductance chloride channel on pancreatic duct cells. *Am. J. Physiol.* **259:**C752–C761
15. Gray, M.A., Plant, S., Argent, B.E. 1993. cAMP-regulated whole cell chloride currents in pancreatic duct cells. *Am. J. Physiol.* **264:**C591–C602
16. Gray, M.A., Winpenny, J.P., Porteous, D.J., Dorin, J.R., Argent, B.E. 1994. CFTR and calcium-activated chloride currents in pancreatic duct cells of a transgenic CF mouse. *Am. J. Physiol.* **266:**C213–221
17. Grassl, S.M., Aronson, P.S. 1986. Na^+/HCO_3^- cotransport in basolateral membrane vesicles isolated from rabbit renal cortex. *J. Biol. Chem.* **261:**8778–8783
18. Gross, E., Hopfer, U. 1998. Voltage and cosubstrate dependence of the Na-HCO_3 cotransporter kinetics in renal proximal tubule cells. *Biophys. J.* **75:**810–824
19. Hartmann, T., Verkman, A.S. 1990. Model of ion transport regulation in chloride-secreting airway epithelial cells. *Biophys. J.* **58:**391–401
20. Hellmessen, W., Christian, A.L., Fasold, H., Schulz, I. 1985. Coupled Na^+-H^+ exchange in isolated acinar cells from rat exocrine pancreas. *Am. J. Physiol.* **249:**G125–G136
21. Hoffman, E.K., Simonsen, L.O. 1989. Membrane mechanisms in volume and pH regulation in vertebrate cells. *Physiol. Rev.* **69:**315–382
22. Ishiguro, H., Naruse, S., Steward, M.C., Kitagawa, M., Ko, S.B.H., Hayakawa, T., Case, R.M. 1998. Fluid secretion in interlobular ducts from guinea-pig pancreas. *J. Physiol.* **511.2:**407–422
23. Ishiguro, H., Steward, M.C., Lindsay, A.R.G., Case, R.M. 1996. Accumulation of intracellular HCO_3^- by Na^+-HCO_3^- cotransport in intracellular ducts from guinea-pig pancreas. *J. Physiol.* **495.1:**169–178
24. Ishiguro, H., Steward, M.C., Wilson, R.W., Case, R.M. 1996. Bicarbonate secretion in interlobular ducts from guinea-pig pancreas. *J. Physiol.* **495.1:**179–191
25. Kohn, O.F., Mitchell, P.P., Steinmetz, P.R. 1990. Characteristics of apical Cl-HCO_3 exchanger of bicarbonate-secreting cells in turtle bladder. *Am. J. Physiol.* **258:**F9–F14
26. Linsdell, P., Tabcharani, J.A., Hanrahan, J.W. 1997. Multi-ion mechanism for ion permeation and block in the cystic fibrosis transmembrane conductance regulator chloride channel. *J. Gen. Physiol.* **110:**365–377
27. Mahieu, I., Becq, F., Wolfensberger, T., Gola, M., Carter, N., Hollande, E. 1994. The expression of carbonic anhydrases II and IV in the human pancreatic cancer cell line (Capan-1) is associated with bicarbonate ion channels. *Biol. Cell* **81:**131–141
28. Novak, I., Greger, R. 1988. Electrophysiological study of transport systems in isolated perfused pancreatic ducts: properties of the basolateral membrane. *Pfluegers Arch.* **411:**58–68
29. Novak, I., Greger, R. 1988. Properties of the luminal membrane of isolated perfused rat pancreatic ducts: effects of cyclic AMP and blockers of chloride transport. *Pfluegers Arch.* **411:**546–553
30. Novak, I., Greger, R. 1991. Effects of bicarbonate on potassium conductance of isolated perfused rat pancreatic ducts. *Pfluegers Arch.* **419:**76–83
31. O'Reilly, C.M., Winpenny, J.P., Argent, B.E., Gray, M.A. Cystic fibrosis transmembrane conductance regulator in guinea-pig pancreatic duct cells and their inhibition by bicarbonate ions. *Gastroenterology* (*in press*)
32. Poulsen, J.H., Fischer, H., Illek, B., Machen, T.E. 1994. Bicarbonate conductance and pH regulatory capability of cystic fibrosis transmembrane conductance regulator. *Proc. Natl. Acad. Sci.* **91:**5340–5344
33. Rakowski, R.F. 1993. Charge movement by the Na/K pump in *Xenopus* oocytes. *J. Gen. Physiol.* **101:**117–144
34. Seki, G., Coppola, S., Froemter, E. 1993. The Na^+-HCO_3^- cotransporter operates with a coupling ratio of 2 HCO_3^- to 1 Na^+ in isolated rabbit renal proximal tubule. *Pfluegers Arch.* **425:**409–416
35. Sjaastad, M.D., Wenzl, E., Machen, T.E. 1992. pH_i dependence of Na-H exchange and H delivery in IEC-6 cells. *Am. J. Physiol.* **262:**C164–C170
36. Sohma, Y., Gray, M.A., Imai, Y., Argent, B.E. 1996. A mathematical model of the pancreatic ductal epithelium. *J. Membrane. Biol.* **154:**53–67
37. Sohma, Y., Gray, M.A., Imai, Y., Argent, B.E. 1997. Regulation of anion secretion by cyclic AMP and Ca^{2+} in a computer model of the rat pancreatic ductal epithelium. *J. Physiol.* (Abstr.) **499.P:**31P
38. Spring, K.R. 1983. Fluid transport by gallbladder epithelium. *J. Exp. Biol.* **106:**181–194
39. Steward, M.C., Garson, M.J. 1985. Water permeability of *Necturus* gallbladder epithelial cell membranes measured by nuclear magnetic resonance. *J. Membrane Biol.* **86:**203–210
40. Strange, K., Spring, K.R. 1987. Cell membrane permeability of rabbit cortical collecting duct. *J. Membrane Biol.* **96:**27–43
41. Stuenkel, E.L., Machen, T.E., Williams, J.A. 1988. pH regulatory mechanisms in rat pancreatic ductal cells. *Am. J. Physiol.* **254:**G925–G930
42. Toennessen, T.I., Sandvig, K., Olsenes, S. 1990. Role of Na^+-H^+ and Cl^--HCO_3^- antiports in the regulation of cytosolic pH near neutrality. *Am. J. Physiol.* **258:**C1117–C1126
43. Veel, T., Villanger, O., Holthe, M.R., Cragoe, E.J. Jr., Raeder, M.G. 1990. Na^+-H^+ exchange is not important for pancreatic HCO_3^- secretion in the pig. *Acta Physiol. Scand.* **144:**239–246

44. Weinstein, A.M., Stephenson, J.L. 1979. Electrolyte transport across a simple epithelium. Steady-state and transient analysis. *Biophys. J.* **27:**165–187
45. Wu, M.M., Civan, M.M. 1991. Voltage dependence of current through the Na,K-exchange pump of *Rana* oocytes. *J. Membrane Biol.* **121:**23–36
46. Zhao, H., Star, R.A., Muallem, S. 1994. Membrane localisation of H^+ and HCO_3^- transporters in the rat pancreatic duct. *J. Gen. Physiol.* **104:**57–85

Appendix A

Derivation of the Turnover Rates of the Na^+-HCO_3^- Cotransporter and the H^+ Pump

Na^+-HCO_3^- Cotransporter

Based on the assumptions for the Na^+-HCO_3^- cotransporter (i)–(v) (*see* Methods), the equations shown below were derived.

$$[E_o][Na^+]_{bl} = K_{cNa} \cdot [E_oNa^+] \tag{A1}$$

$$[E_oNa^+][HCO_3^-]_{bl}^n = K_{cHCO3}^n \cdot [E_oNa^+nHCO_3^-] \tag{A2}$$

$$[E_i] \cdot [Na^+]_c = K_{cNa} \cdot [Na^+E_i] \tag{A3}$$

$$[Na^+E_i] \cdot [HCO_3^-]_c^n = K_{cHCO3}^n \cdot [nHCO_3^-Na^+E_i] \tag{A4}$$

$$[E_o] + [E_oNa^+] + [E_oNa^+nHCO_3^-] + [E_i] + [Na^+E_i] + [nHCO_3^-Na^+E_i] = [E_t] \tag{A5}$$

$$J_{Na\text{-}HCO3} = l_f \cdot [E_oNa^+nHCO_3^-] - l_b \cdot [nHCO_3^-Na^+E_i] = k_f \cdot [E_i] - k_b \cdot [E_o] \tag{A6}$$

where

$$l_f = P_l \cdot \exp(-(1 - n + zL) \cdot F \cdot PD_{bl}/2RT) \tag{A7}$$

$$l_b = P_l \cdot \exp((1 - n + zL) \cdot F \cdot PD_{bl}/2RT) \tag{A8}$$

$$k_f = P_k \cdot \exp(zL \cdot F \cdot PD_{bl}/2RT) \tag{A9}$$

$$k_b = P_k \cdot \exp(-zL \cdot F \cdot PD_{bl}/2RT) \tag{A10}$$

$$zL = n - 1 \tag{A11}$$

From equations (A1)–(A11), the turnover rate of the Na^+-HCO_3^- cotransporter ($J_{Na\text{-}HCO3}$), can be expressed as shown in Eq. (3).

H^+ Pump

Based on the assumptions for the H^+ pump (i)–(iv) (*see* Materials and Methods), the equations below were derived.

$$[E_o][H^+]_{bl}^n = K_{Hpbl} \cdot [E_onH^+] \tag{A12}$$

$$[E_i][H^+]_c^n = K_{Hpc} \cdot [nH^+E_i] \tag{A13}$$

$$[E_o] + [E_onH^+] + [E_i] + [nH^+E_i] = [E_t] \tag{A14}$$

$$J_{Hpump} = l_f[nH^+E_i] - l_b[E_onH^+] = k_f[E_o] - k_b[E_i] \tag{A15}$$

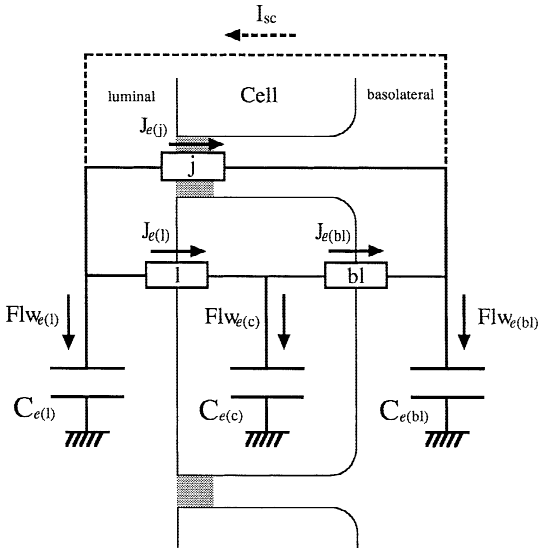

Fig. B1. Electrical equivalent circuit used for calculating membrane potentials and short-circuit current in the model. $C_{e(k)}$ (k = *l*, *c*, *bl*) represents a conceptual capacitor (and its capacitance) corresponding to each compartment. Open rectangles represent the transport element carrying electrical charge (a voltage-dependent current source) on luminal (*l*), basolateral (*bl*) and paracellular (*j*) pathways, respectively. $J_{e(m)}$ is the total flux of positive charge through a membrane (m). $Flw_{e(k)}$ is the net influx of positive charge into a compartment (k). Under the short-circuit condition, I_{sc} flows from $C_{e(bl)}$ to $C_{e(l)}$ (indicated by the dashed line). *See* text for details.

where

$$l_f = P_{lf} \cdot \exp(n \cdot F \cdot PD_{bl}/2RT) \tag{A16}$$

$$l_b = P_{lb} \cdot \exp(-n \cdot F \cdot PD_{bl}/2RT) \tag{A17}$$

$$k_f = P_k \tag{A18}$$

$$k_b = P_k \tag{A19}$$

From equations (A12)–(A19), the turnover rate of the H^+ pump (J_{Hpump}), can be expressed as shown in Eq. (4).

Appendix B

Calculation of Membrane Potential and Short-Circuit Current

Although our modeling technique is based on conventional methods (e.g., ref. 44), we have employed an electrical equivalent circuit for calculating membrane potentials and short-circuit current.

Membrane Potential

Figure *B*1 shows the electrical equivalent circuit we employed for calculating the membrane potential difference (PD_m), and the short-circuit current (I_{sc}). The circuit consists of three voltage-dependent current sources, corresponding to membrane transport elements on each

membrane, and three conceptual capacitors corresponding to each compartment. This equivalent circuit is simple and its electrical behavior is easy to describe numerically.

$$J_{e(bl)} + J_{e(j)} = Flw_{e(bl)} = C_{e(bl)} \cdot \left(\frac{dE_{(bl)}}{dt} \right) \tag{B1}$$

$$J_{e(l)} - J_{e(bl)} = Flw_{e(c)} = C_{e(c)} \cdot \left(\frac{dE_{(c)}}{dt} \right) \tag{B2}$$

$$-J_{e(l)} - J_{e(j)} = Flw_{e(l)} = C_{e(l)} \cdot \left(\frac{dE_{(l)}}{dt} \right) \tag{B3}$$

where $J_{e(m)}$ is total flux of positive charge through a membrne (m), $Flwe_{e(k)}$ is net influx of positive charge into a compartment (k), and $C_{e(k)}$ is the conceptual electrical capacitance of a compartment (k).

Note that we used a same value for $C_{e(l)}$, $C_{e(c)}$ and $C_{e(bl)}$.

$$C_{e(l)} = C_{e(c)} = C_{e(bl)} \tag{B4}$$

The potential of each compartment was calculated as a charge to the conceptual capacitor using equation (5*d*). The circuit is equilibrated when all the capacitors are fully charged, and the electric currents into each capacitor are zero ($Flw_{e(k)} = 0$). Therefore, from Eqs. (*B*1)–(*B*3):

$$J_{e(l)} = J_{e(bl)} = -J_{e(j)} \tag{B5}$$

The situation described by Eq. B5 corresponds to the open-circuit condition. The potential differences between the conceptual capacitors (ΔE), corresponds to each membrane potential difference (PD).

Changing the transport parameters induces transient net electric flows into the compartments until the equivalent circuit is re-equilibrated ($Flw_{e(k)} = 0$, which means that the cation influx and the anion influx into each compartment are equally balanced).

In this method, $C_{i(k)}$ should be set a value small enough to maintain electroneutrality of the intracellular compartment and to avoid a delay in the potential change. The computer program calculated the model equations with four different values of $C_e = 8 \times 10^{-5}$, 8×10^{-6}, 8×10^{-7} and 8×10^{-8} F/cm^2 epithelium using the double precision data type and compared the simulated results at each C_e value. We confirmed that decreasing C_e 10-fold ($C_e = 8 \times 10^{-6}$ *F*), 100-fold ($C_e = 8 \times 10^{-7}$ *F*) and 1,000-fold ($C_e = 8 \times 10^{-8}$ *F*) had no significant effect on the transient time courses and the steady-state values of the model variables calculated with $C_e = 8 \times 10^{-5}$ *F*. This insensitivity of the simulated results to a change in C_e over the nano- to micro-farad range means that these C_e values are small enough to maintain intracellular electroneutrality allowing us to calculate the model variables with a good accuracy. In this method, membrane potential change induces a small but certain deviation from electroneutrality (e.g., with 2 μEq throughout all simulations with $C_e = 8$ μ*F*). However, we should note that biological membranes actually have an electrical capacitance of microfarads per cm^2 [7] and that membrane potential change might induce some deviation from the electroneutrality even in natural living cells.

Short-Circuit Current

To simulate the short-circuit condition, we applied a current (I_{sc}) from the basolateral to the luminal compartment. I_{sc} is defined as a current required for setting the transepithelial potential difference ($PD_{te} = E_{(bl)} - E_{(l)}$) to 0 mV as below:

$$I_{sc} = \left(\frac{E_{(bl)} - E_{(l)}}{1/C_{e(bl)} + 1/C_{e(l)}} \right) \Big/ dt \tag{B6}$$

At the beginning of the first *dt* interval of the short-circuit condition, $E_{(bl)}$ is not equal to $E_{(l)}$ because the model was under the open-circuit condition in the previous *dt* interval. Therefore, I_{sc} in the first *dt* interval of the short-circuit condition is not the so-called 'short-circuit current', but an initial current required for setting the model epithelium to the short-circuit condition (cancelling the transepithelial potential difference).

In the later *dt* intervals of the short-circuit condition, PD_{te} is already set to 0 mV ($E_{(bl)} = E_{(l)}$) at the beginning of each interval. Therefore, I_{sc} is equal to the total transepithelial current driven by the model epithelium and derived from Eq. (*B1*) and Eq. (5*d*) as below:

$$\begin{aligned} I_{sc} &= \left\{ \frac{(E_{(bl),t} + Flw_{e(bl)} \cdot dt/C_{e(bl)}) - (E_{(l),t} + Flw_{e(l)} \cdot dt/C_{e(l)})}{1/C_{e(bl)} + 1/C_{e(l)}} \right\} \Big/ dt \\ &= \left(\frac{Flw_{e(bl)} \cdot dt/C_{e(bl)} - Flw_{e(l)} \cdot dt/C_{e(l)}}{1/C_{e(bl)} + 1/C_{e(l)}} \right) \Big/ dt \\ &= \frac{Flw_{e(bl)}/C_{e(bl)} - Flw_{e(l)}/C_{e(l)}}{1/C_{e(bl)} + 1/C_{e(l)}} \end{aligned} \tag{B7}$$

where t is a time in the later *dt* intervals under the short-circuit condition, and $E_{(l),t}$ and $E_{(bl),t}$ are potentials of luminal and basolateral compartments at the time t, respectively. Note that $E_{(l),t}$ is equal to $E_{(bl),t}$($PD_{te,t} = 0$) (*see above*).

In this study we used a same value for $C_{e(l)}$, $C_{e(c)}$ and $C_{e(bl)}$ (Eq. (B4)). Therefore, from Eq. (B7):

$$I_{sc} = \frac{Flw_{e(bl)} - Flw_{e(l)}}{2} \tag{B8}$$